Icarus 392 (2023) 115393

Contents lists available at ScienceDirect

Icarus

journal homepage: www.elsevier.com/locate/icarus

# Characterisation of deposited dust particles on Mars insight lander Instrument Context Camera (ICC) lens

H. Chen-Chen [a,*], S. Pérez-Hoyos [a], A. Sánchez-Lavega [a], J. Peralta [b]

[a] Departamento de Física Aplicada, Escuela de Ingeniería de Bilbao, Universidad del País Vasco (UPV/EHU), Bilbao 48013, Spain
[b] Departamento de Física Atómica, Molecular y Nuclear, Facultad de Física, University of Sevilla, Spain

ARTICLE INFO

*Keywords:*
Mars
InSight
ICC
Dust particles on lens
Aeolian transport

ABSTRACT

The ubiquitous dust in the Martian environment plays a key role in its weather and climate: it must be taken into account in the interpretation of remote sensing data and observations, and could pose a potential risk to surface equipment and operations. In this study, we use observations retrieved by the Instrument Context Camera (ICC) onboard the InSight lander to evaluate the accumulation of dust on the camera lens and estimate the size of the deposited dust particles. Dust contamination is revealed as mottled pattern image artefacts on ICC observations. These were detected using a template matching blob detection algorithm and modelled with a first-order optical model to simulate their size and optical density as a function of the particle diameter. The results show a deep decay in the first 70 sols ($L_S$ = 295–337°, MY34) during which dust particles deposited at landing were mostly removed. The subsequent gradual decrease and stable behaviour in the number of detected particles is only interrupted by accumulation and removal periods around sols 160 ($L_S \sim 23°$, MY35) and 800–1100 ($L_S$ = 9–150°, MY36). The estimated particle sizes follow a similar trend, with deposited particles due to wind-driven forces (average diameter < 50 μm) being smaller than the ones deposited by other forces during landing, with particles of up to 220 μm of diameter. The results of this study provide an additional source of information for evaluating aeolian dust processes in Mars, with quantitative results on dust accumulation and removal activity, and may contribute to a better determination of dust entrainment threshold models by constraining susceptible dust particle sizes.

## 1. Introduction

The environment of Mars is partly characterised by the ubiquitous atmospheric and surface dust. This dust is lifted from the surface, transported and removed through a complex interplay of mechanisms that include: atmospheric settling, dust storms, convective vortices (dust devils) and other aeolian processes (Perko et al., 2002; Kok et al., 2012).

The properties and dynamics of aeolian dust are relevant for multiple reasons: airborne dust has implications in the atmospheric heating rates and dynamics, playing a key role in the weather and climate of Mars, similarly to water in the terrestrial atmosphere (Kahre et al., 2017); surface dust deposits must be taken into account for the correct interpretation of remote sensing data and in situ observations of surface materials (Golombek et al., 2008; Herkenhoff et al., 2008); and finally, dust deposition poses a potential risk to the correct functioning and survival of the equipment and instrumentation operating on Mars through obscuration of solar panels, wearing of moving parts, contamination of optics or modification of thermal properties, and may limit mission duration (Perko et al., 2002). Thus, the continued study of the composition of Martian dust, particle properties, transport processes and mechanisms by which dust is deposited in equipment and instrumentation surfaces is a relatively high priority issue within the robotic and human Mars exploration programme (Levine et al., 2018).

The best available data on Martian dust properties come from observations in the visible and infrared wavelength region retrieved by landers, rovers, and orbiters (e.g. Perko et al., 2002; Smith, 2008; Herkenhoff et al., 2008; Kahre et al., 2017). In situ observations of dust deposition, accumulation and removal processes, and the characterisation of dust particle properties were first retrieved by the Viking Landers' cameras, which detected surface changes, erosion and modification of surface material in the lander-disturbed areas during a dust storm event (Arvidson et al., 1983), observing individual particle sizes (diameters) of about 2 mm and up to 40 mm for agglomerates (Arvidson et al., 1989); whereas grain size estimates of 2–10 μm were inferred from

* Corresponding author.
*E-mail address:* hao.chen@ehu.eus (H. Chen-Chen).

https://doi.org/10.1016/j.icarus.2022.115393
Received 20 May 2022; Received in revised form 17 November 2022; Accepted 3 December 2022
Available online 8 December 2022

the Viking Gas Exchange experiment (Moore et al., 1987) and atmospheric dust with airborne particle size distribution effective radius of 1.5–1.8 μm (Pollack et al., 1995) were estimated.

In the Mars Pathfinder mission, the passive accumulation of air-fall dust on the camera calibration target and on the lander solar cell arrays were evaluated to estimate the atmospheric dust settling rates (Johnson et al., 2003; Landis and Jenkins, 2000). Atmospheric dust properties were inferred by analysing the Martian sky brightness in Sun-pointing sequences returned by the Imager for Mars Pathfinder, resulting in airborne particle size distribution effective radius of 1.6–1.7 μm (Tomasko et al., 1999; Markiewicz et al., 1999). On the other hand, observations of the wheel tracks left by Pathfinder's Sojourner rover were largely consistent with loose material with grain diameters of <40 μm (The Rover Team, 1997), similar to the 30–40 μm dust sizes inferred from the wheel abrasion experiment (Ferguson et al., 1999). For the Mars Exploration Rovers (MER), movement of sand-size grains and its accumulation on the Spirit rover deck were reported by Greeley et al. (2006), the erasure and modification of rover tracks by dust deposition were observed by both rovers within a few sols (Geissler et al., 2010), and several dust accumulation and cleaning events were detected and evaluated using the Pancam calibration target and monitoring of solar array performance (Kinch et al., 2007, 2015; Vaughan et al., 2010; Stella and Herman, 2010). MER surface studies identified the dominant soil type as 'dark grains' with sizes of up to 100 μm (Yen et al., 2005). Further particle size estimations from thermal inertia measurements with the Miniature Thermal Emission Spectrometer (Mini-TES) onboard the two rovers were consistent, with particle diameters of 45 and 160 μm (Fergason et al., 2006). Observations retrieved by the Microscopic Imager (MI), with a capacity of accurately measuring single grain diameters of 100 μm, constrained the particle size distribution at different sites through the MER mission (Herkenhoff et al., 2019, and references therein) and estimated dust particle sizes located on the rover body, calibration target and solar arrays (Herkenhoff et al., 2008; Landis et al., 2006). MI images revealed that dust particles on the rover cohere and form large aggregates of up to several mm, while calibration target grains present a range from assumed (unresolved) diameters of <4 μm to 250 μm (sand size), and showed that the latter ones could saltate to a rover deck height of 70 cm in strong winds (Vaughan et al., 2010). MER atmospheric dust size estimations using direct Sun-imaging sequences with the solar filters of the Pancam instrument returned airborne dust particle effective radius of about 1.5 μm (Lemmon et al., 2004). In the Mars Science Laboratory (MSL) mission, the Rover Environmental Monitoring Station (REMS) photodiode sensors were used to monitor the accumulation and removal of dust from the sensor windows located on the Curiosity rover deck, showing seasonal-related cycles (Vicente-Retortillo et al., 2018). The Mars Hand Lens Imager (MAHLI) recorded dust accumulation on various hardware elements throughout the mission, including a planet-encircling dust event in June–July 2018 (Yingst et al., 2020), during which MSL Mast Camera (Mastcam) airborne dust particle size retrievals estimated particle effective radius variations from usual values near 1.5 μm up to 8.0 μm (Lemmon et al., 2019). The Curiosity rover studied the textures and compositions of aeolian sands in the active dune fields of the landing site, observing very fine to medium sized sands (~45 to 500 μm) and with rounded to sub-rounded shapes (Ehlmann et al., 2017). The optical microscope onboard the Phoenix lander returned colour images of soil particles and characterised the particle size distribution with two distinct peaks: below 10 μm (fines) and in the range of 20–100 μm (grains), with most sand grains presenting a sub-rounded shape (Goetz et al., 2010; Pike et al., 2011). Dust settling rates on the solar arrays of this 152-sol Phoenix mission are reported in Drube et al. (2010). The increase of solar power output during the last ~50 sols was associated with higher levels of vortex and dust devil activity, which may have led to dust removal from the panels (Lorenz et al., 2021b). On the other hand, dust accumulation on the solar arrays of the NASA Interior Exploration using Seismic Investigations, Geodesy and Heat Transport (InSight) lander caused an unmitigated degradation in the electrical output throughout the first 800 sols of the mission, with an average decline of 0.2% per sol and no prominent events, and led to visible dustiness of the arrays (Lorenz et al., 2020, 2021a).

However, passive settling is not the only mechanism that contributes to dust deposition, as observations retrieved from landers and rovers reveal dust adhering to vertical or near-vertical surfaces (Yingst et al., 2020). In addition, while dust accumulation and removal on horizontal surfaces has been thoroughly studied (e.g. Kinch et al., 2015; Lorenz et al., 2021b), this is not well-characterised for vertical surfaces due to the absence of systematic, quantifiable observations of dust cover changes (Yingst et al., 2020).

The Instrument Context Camera (ICC) on the InSight lander is a 'fisheye' lens colour camera, with a 124°×124° field of view (FOV), mounted on the edge of the lander body, underneath the top deck. ICC images have been used for selecting the deployment locations of InSight seismometer and heat flow probe instruments (Banerdt et al., 2020; Golombek et al., 2020b), monitoring the deployment activities, and documenting the state of the instruments and workspace (Maki et al., 2018, 2019); as well as for scientific purposes such as the estimation of the atmospheric dust opacity (Spiga et al., 2018; Banfield et al., 2020), analysis of landing site surface physical properties and observation of aeolian surface changes (Charalambous et al., 2021; Perrin et al., 2020).

In this study, we use ICC images to evaluate the accumulation of dust on the camera lens and estimate the size of the deposited dust particles. Dust contamination on the lens reveals as mottled pattern image artefacts. We detect these artefacts on ICC images and use an optical model to simulate the size and optical density of the artefacts. This retrieval contributes to a better understanding of aeolian dust processes on Mars by providing additional quantitative results on dust accumulation and removal activity at InSight's landing site, and constraining susceptible dust grain sizes in wind-driven motion threshold shear velocity models.

This manuscript is structured as follows. In Section 2 we present the observational data used in this work and describe the retrieval algorithm for detecting image artefacts produced by dust particles and the optical model used for the characterisation of the detected dust artefacts. The results of this work are reported in Section 3 and a discussion on the outcomes and their implications is provided in Section 4. Finally, in Section 5 we summarise the main findings of this study and we lay out future research prospects derived from this work.

## 2. Data and methods

### 2.1. InSight ICC images

The ICC is a modified flight spare version of the Hazard Avoidance Camera (Hazcam) onboard the MSL *Curiosity* rover (Maki et al., 2012), which flew build-to-print copies of MER mission engineering cameras (Maki et al., 2003). This 124° × 124° FOV fisheye lens camera shares nearly identical properties as the MSL versions, except for the detector and filter, which were converted from gray-scale to colour by replacing the MSL detector with a Bayer colour filter array version of the same type of frame transfer charge-coupled devices (CCDs). The main properties are summarised in Table 1 (see Maki et al., 2018, for a detailed description of InSight cameras).

The ICC is mounted on the lander body underneath the top deck. The height to the surface of the ICC in the landed setting on Mars may differ slightly from the reported height of 0.77 m in the pre-landing setting (Maki et al., 2018), as there are evidences of footpads sliding and lander tilting (Golombek et al., 2020a, 2020b). The camera is pointing at −41.3° of elevation and 180.1° in azimuth with respect to the local site frame (Deen et al., 2020) and covers the entire deployment workspace of InSight instruments (Fig. 1, panel a).

ICC observations have been retrieved regularly since the start of the mission (sol 0, $L_S = 296°$, MY34; 26th November 2018), accumulating a database of around 2600 images by sol 1200 ($L_S \sim 207°$, MY36; 12th

**Table 1**
Instrument Context Camera (ICC) properties.

| Instrument Context Camera (ICC) | |
|---|---|
| Angular resolution at the centre of the FOV | 2.1 mrad/pixel |
| Focal length | 5.58 mm |
| *f*/number | 15 |
| Entrance pupil diameter | 0.37 mm |
| Field of view | 124 × 124 degrees |
| Diagonal FOV | 180 degrees |
| Depth of field | 0.10 m – infinity |
| Best focus | 0.5 m |
| Spectral range | ~ 400–700 nm |
| Bandpass centres (approximate) | R (600 nm), G (550 nm), B (500 nm) |
| Pixel size | 12 × 12 μm |
| Photosensitive area | 1024 × 1024 pixels |
| Height above surface [a] | 0.77 m |

[a] Pre-landing setting reported height (Maki et al., 2018).

April 2022). In this study, we used the first order Engineering Data Record (EDR) data products generated by the ICC, which correspond to the raw, un-calibrated, uncorrected image data acquired by the camera (see Deen et al., 2020 for details on InSight cameras data products). Only those image files with an image quality index for on-board data compression equal or >95 were considered (see Deen et al., 2020, Appendix C). First order images were selected instead of other derived data products, e.g. radiometrically corrected images, as the use of physical units (radiance) was not required and to avoid possible data modifications due to the image calibration process.

ICC observations are mainly distributed into two groups: local noon observations, between 11 and 13 h local true solar time (LTST), representing 27.5% of the total number of images, and afternoon observations (16–18 h LTST), with 32.6% of the dataset. Due to the forward scattering of direct sunlight in the atmosphere, the region closely surrounding the solar disc, i.e. the solar aureole or circumsolar region, looks very bright: this affects the image's dynamic range and makes it impossible to discern the small spot brightness differences in the 8-bit (0–255 range) images with a strong sky brightness gradient. We used the CAHVOR camera model information (Yakimovsky and Cunningham, 1978; Gennery, 2006) and the labelled solar azimuth and elevation angles to calculate the azimuth, elevation and scattering angles observed by each pixel of the image (Fig. 1, panel a). Those ICC observations containing scattering angles, i.e. angular distances from the centre of the Sun, lower than 10° were discarded from this study. This resulted in an observation data set of 2102 images for 819 different sols covering from sol 1 to 1200. The full list of ICC images is provided in the supplementary material.

### 2.2. Detection of image artefacts

The detection of dust produced artefacts in ICC images may be regarded as a blob detection task, common in the pattern recognition field within computer vision, which focuses on finding regions in an image that differ in properties (brightness, colour, shape, etc.) compared to the surrounding region (e.g., Lindeberg, 1993). In the current case, a blob is defined as a region with at least one local extremum, such as a bright spot in a dark image or a dark spot in a light image (Lindeberg, 1993).

Our selected blob detection method is the template matching via the normalized cross-correlation (NCC) (Lewis, 1995; Briechle and Hanebeck, 2001; Tsai and Lin, 2003), which determines the position of a given template or feature in an image by measuring the similarity between the template and the image, for all the point of the images, as:

$$NCC(u,v) = \frac{\sum_{x,y} f(x,y)\, t(x-u, y-v)}{\sqrt{\sum_{x,y}\left[f(x,y) - \bar{f}_{u,v}\right]^2 \sum_{x,y}\left[t(x-u,y-v) - \bar{t}\right]^2}}, \quad (1)$$

where $f$ is the image, the sum is over $x$, $y$ under the window containing the template $t$ positioned at $u$, $v$, $\bar{t}$ is the mean of the template and $\bar{f}_{u,v}$ is the mean of the image in the region under the template.

In this study, only the sky region of an ICC observation (~33% of the 1024 × 1024 image) were considered for performing the blob detection, as the multiple and diverse features of the ground area, such as rocks, mission instruments, lander parts, shadows and variable illumination conditions and albedo, would vastly complicate the detection task. This same target region, covering the ground area and the above-horizon area of the ICC images, were previously evaluated by Charalambous et al. (2021) using an image differencing approach to identify and rank-order dust removal events. It is also noted that part of the lander structure is permanently present on the upper-left corner of the ICC observations, obstructing part of the sky above the horizon and which shall be masked out before performing any image analysis.

Thus, image artefacts produced by dust on the sky were assumed as dark-on-bright, out-of-focus spots with a soft intensity transition (e.g., Dirik et al., 2008), as it can be appreciated from the detailed views of ICC image dataset, especially within the first 70 sols (Fig. 1, left column). Based on this, a Gaussian-type intensity loss model was selected as the template model for the NCC calculations in the form of the 2-Dimensional (2D) Gaussian function of:

$$t(x,y) = -A \cdot exp\left(-\frac{1}{2}\frac{\left((x-w)^2 + (y-w)^2\right)}{\sigma^2}\right), \quad (2)$$

$$x, y = 0, 1, \ldots, 2w$$

where $A$ is optical density, i.e. brightness decay, in the pixel produced by the blob in units of digital numbers (DN), $\sigma$ is the standard deviation of the Gaussian distribution, and $2w$ is the width of the template.

The result of the NCC method is a 2D map of values, where each value is computed via the expression (1) by cross-correlating the Gaussian dust model template (2) with a window of size $2w \times 2w$ sliding over all pixel positions of the image (Fig. 2). The NCC returned values are within the interval [−1,1] where 1 means highest correlation. In the NCC output, values higher than an empirically set threshold were selected to locate the regions where the template best matches the image, i.e. location of the local maxima (e.g., Dirik et al., 2008; Sierra et al., 2017).

The template matching-based method is likely to detect some scene-dependent intensity degradations as dust produced artefacts. In order to reduce false detections, the template matching scheme was followed by additional examinations of the intensity loss and its spatial decay characteristics of each dust blob candidate by fitting the template-based 2D Gaussian distribution function using a non-linear least-square minimisation algorithm (Newville et al., 2014) to retrieve the best fitting $A$ and $\sigma$ values. If the resulting values are within a preset interval, the detected blob was tagged as dust produced artefact.

### 2.3. Optical model

The optics-based model presented in Willson et al. (2005) was used for simulating the size and optical density of image artefacts produced by dust particles deposited on the ICC lens. The model follows the path of light collected by the lens for a single pixel and considers how dust particles on the lens affect the light reaching the pixel. The 'pixel collection cone' is defined as the solid angle subtended by a pixel, if a dust particle absorbs or scatters light away from this collection cone, the light reaching the pixel will be decreased by a factor equal to the fraction of the collection cone blocked by the particle (see Willson et al., 2005 for a detailed description).

The diagram of the model is shown in the top panel of Fig. 3. The parameters of the model correspond to the object and image distances, $s$ and $s'$, respectively, which are related with the focal length, $f$, by the

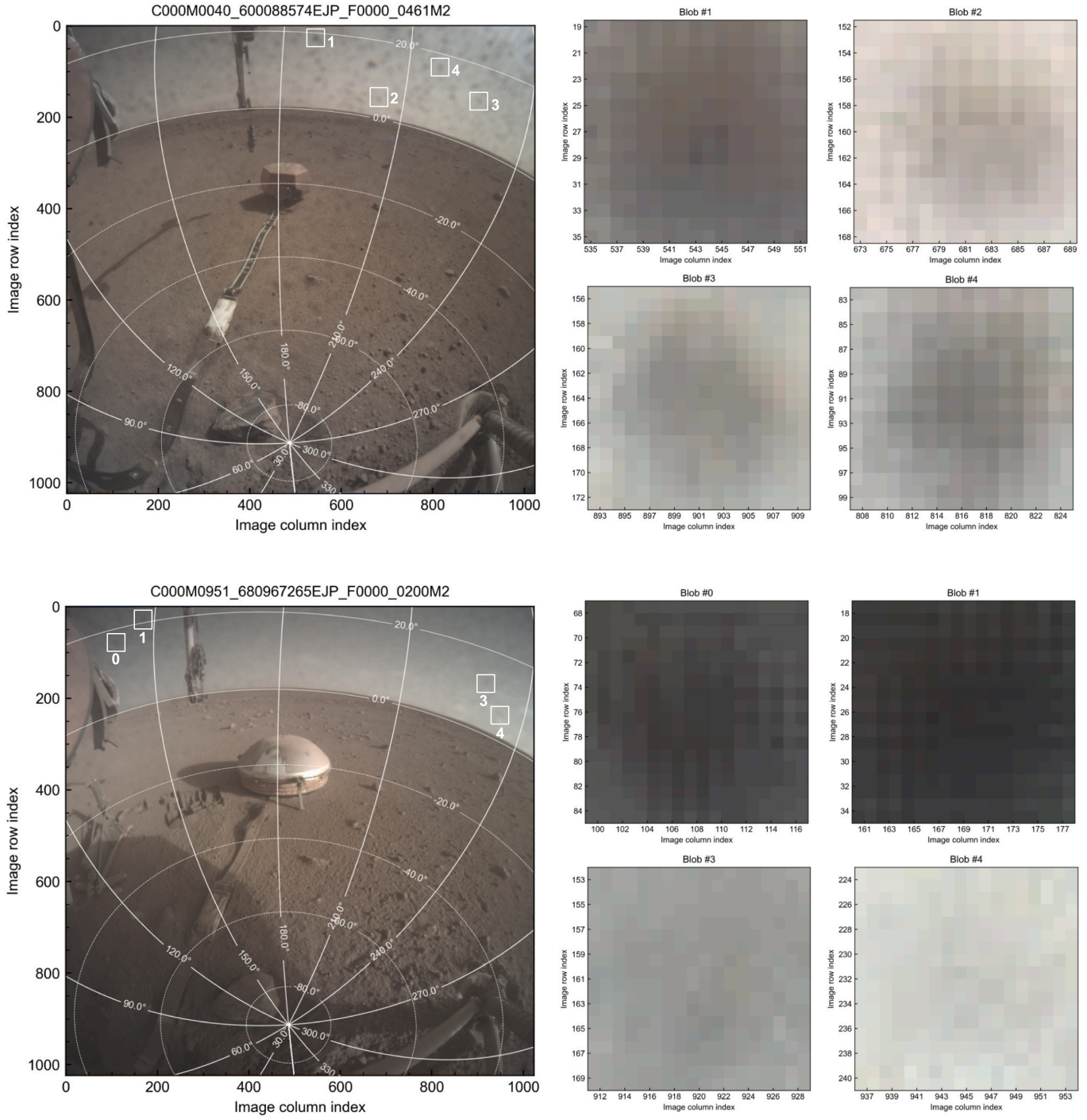


**Fig. 1.** ICC observations and image artefacts due to dust particles deposited on the lens. Left column: examples of ICC observations retrieved on sol 40 (top panel) and 65 (bottom panel). The grid shows the azimuth and elevation angles of the image in the Mars local level reference system (Maki et al., 2018; Deen et al., 2020). The numbered boxes identify each of the image artefacts shown in detail. Right column: detailed views of image artefacts due to dust particles deposited on the ICC camera's lens. Top panel: observation file C000M0040_600088574EJP_F0000_0461M2, retrieved on sol 65, $L_S = 319.78°$ (MY34) at LTST = 14:27:10. Bottom panel: image file C000M0951_680967265EJP_F0000_0200M2, retrieved on sol 951, $L_S = 79.05°$ (MY36) at LTST = 16:41:32.

relationship $\frac{1}{s} + \frac{1}{s'} = \frac{1}{f}$; the distance between the lens window and the first principal point or front nodal point of the lens, $w$, the diameter of the entrance pupil of the lens, $a$, and the diameter of the entrance pupil on the lens window, $c$, which can be approximated by $c = a\left(1 - \frac{w}{s}\right)$.

The attenuation produced by a dust particle with diameter $d$ and located at $(x_D, y_D)$ on the lens window is calculated as follows. For each pixel position $(x_i, y_i)$ in the image, the position of the intersection of the pixel line-of-sight with the lens window, $(x_w, y_w)$, is determined using similar triangles with $x_w = \frac{w}{s'}x_i$, and $y_w = \frac{w}{s'}y_i$. The attenuation is determined by the overlap area between the dust particle and the collection cone of the pixel (Fig. 3, panel b). For simplicity, both the dust particle and the intersection of the pixel collection cone with the lens window are assumed as circular discs. Thus, the attenuation factor is calculated as the area of overlap between two circles, with diameters $c$ and $d$, with centres $(x_w, y_w)$ and $(x_D, y_D)$; divided by the area of the intersection of the pixel collection cone with the lens window, $\pi\left(\frac{c}{2}\right)^2$.

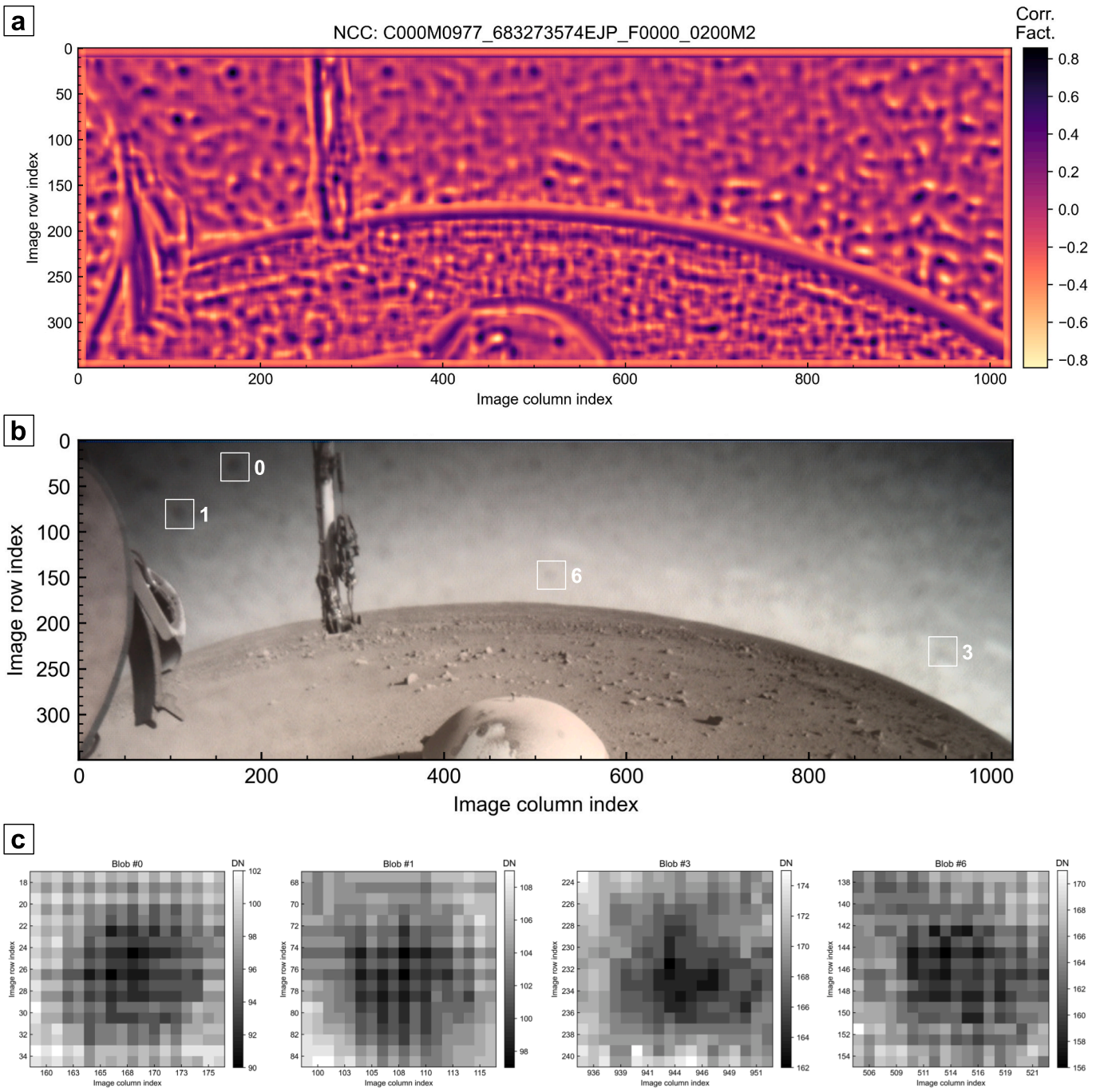


**Fig. 2.** Template matching output and detected dust related blob candidates. (a) Correlation factor results of the normalized cross correlation (NCC) template matching blob detection method for ICC observation C000M0977_683273574EJP_F000_0200M2, retrieved on sol 977 $L_S = 90.77°$ (MY36) at LTST = 16:15:49. (b) In order to facilitate the visual detection and comparison, a contrast-enhanced version of the observations derived using the CLAHE (Contrast Limited Adaptive Histogram Equalization) method is provided, together with the location of some examples of detected blob candidates. (c) Detailed view of the corresponding blob candidates in grayscale and with units of DN.

### 2.4. Methodology

For each ICC observation we proceeded in the following manner:

1. *Load the image*. The ICC image was loaded from the EDR file, together with its relevant label data (e.g. sol number, LTST, $L_S$) and the 1024×1024 Bayer colour-image was converted into grayscale. As the image artefact detection algorithm was applied only over the sky region of the image in order to detect dark-on-bright blobs, the lower part of the image (rows 350 to 1024) was clipped out from the image data array (Fig. 2, panel c).
2. *Mask*. Some non-valid regions were masked out of the image analysis process, these include: the prominent lander body structure on the left border of the image, the surface region in the bottom-half of the image, the removable ICC lens protective cap used during the first 4 sols, and the instrument deployment robotic arm when this was within the FOV of the observation. For the first 3 cases (lander body, surface region, and protective cap) pre-calculated mask arrays were generated by stacking images featuring these elements and applying

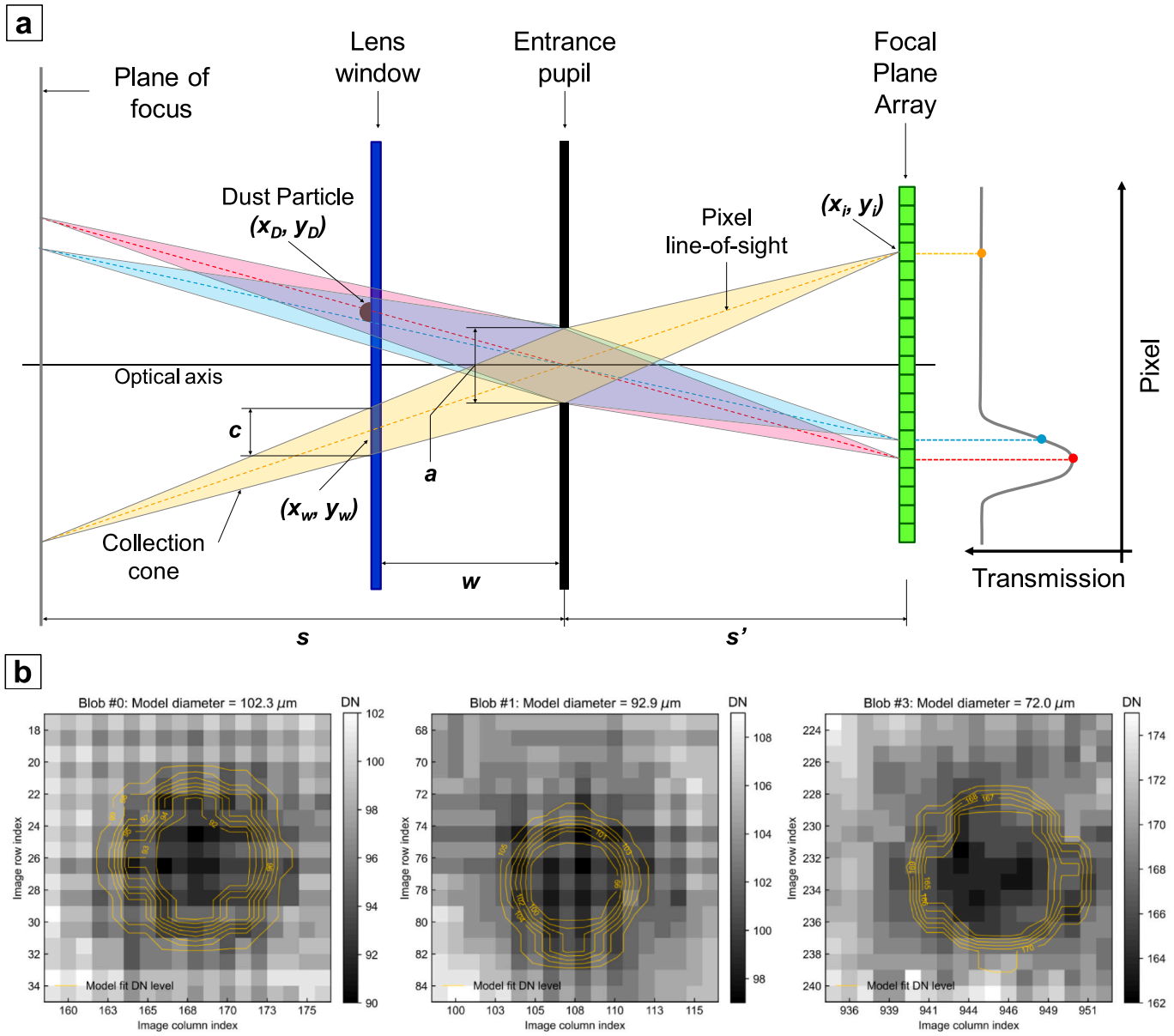


**Fig. 3.** First order optical model for simulating image artefacts produced by dust particles. (a) This diagram shows how the collection cones of three different pixels interact with a dust particle to produce varying transmission values (attenuation) across the detector. Adapted from Willson et al. (2005). (b) Overlay of Willson et al. (2005) optical model result, with yellow contour lines showing equal DN-levels, on 3 detected image artefacts due to dust for observation C000M0977_683273574EJP_F000_0200M2, with model estimated diameter sizes of (left) 102.3 μm, (centre) 92.9 μm, and (right) 72.0 um. (For interpretation of the references to colour in this figure legend, the reader is referred to the web version of this article.)

edge detection algorithms for the segmentation of the valid and non-valid areas (e.g. Bradski, 2000; Canny, 1986; Kroon, 2009). The mask of the robotic arm was created individually for each ICC image: contour detection and segmentation algorithms were also used on the cropped 350×1024 image in order to distinguish between the sky region and other darker regions, including the robotic arm if within the FOV. Finally, the detected contours were cross-checked with the pre-calculated mask to extract the sky region and discard the robotic arm contour (see the detailed process in Section A1 of the supplementary material).

3. *Blob detection* via *template matching*. The NCC 2D-array described by expression (1) was calculated using the template matching algorithm implemented in the scikit-image processing library for Python (Briechle and Hanebeck, 2001; Van der Walt et al., 2014). The input was the 350 ×1024 size grayscale image and the template was generated using expression (2), with preset values for the decay and standard deviation of $A_{NCC} = 1.0$ DN and $\sigma_{NCC} = 0.8$, respectively. Minimum and maximum image blob radius, with values of $r_{min} = 3$ pixels and $r_{max} = 15$ pixels, respectively, were defined in order to constrain the size of the detected artefacts in the image-space. These preset values were empirically derived from the individual analysis and manual count based performance evaluation of the algorithm for a subset of ICC observations for different sols, periods ($L_S$) and scene's lighting (see a detailed description in Section A2 of the supplementary material). The width of the template kernel was then defined after these values as $2w = (r_{min} + r_{max})$. Following these definitions, the list of dust blob candidates was obtained by evaluating the local maxima in the NCC matrix with a non-maximum suppression algorithm (Neubeck and Van Gool, 2006). The segmentation of these potential blobs in non-overlapping squares was

performed by finding the square size for each blob as the minimum value between the half of the image-space distance to the nearest blob and the mean of $r_{min}$ and $r_{min}$ values, while also taking into account the minimum distance of $r_{min} = 3$ pixels (e.g., Mohr et al., 2019; Dirik et al., 2008).

4. *Validation of dust blob candidates.* The first step in the validation of the NCC template matching identified blobs was to discard those blobs with segmented areas containing one or more masked pixels. For each of the remaining blob candidates, its segmented area is fitted by means of a non-linear least squares method (Virtanen et al., 2020) to a 2D-Gaussian function in the form of $f(x,y) = B_{DN} + t(x,y)$, where $B_{DN}$ is the background brightness of the segmented area, in units of DN, and $t(x,y)$ is the function given by expression (2). In this step, valid and non-valid blobs were filtered based on the best-fitting background brightness level, $B_{DN}$, brightness loss, $A$, and the $\sigma$-scale parameter outputs: those blob candidates with background base intensity levels between 1 and 255 DNs, brightness loss DN value greater than a predefined $A_{min} = 2$ DN, and with $\sigma$-scale values resulting in full width at half maximum (FWHM) values between $r_{min} = 3$ pixels and $r_{max} = 15$ pixels, were tagged as valid dust related blobs. These values were derived empirically based in a manual count analysis of the retrieval performance of the algorithm for different sols, periods, and under different lighting conditions (see Section A2 of the supplementary material). A conservative strategy approach was selected to have a low false negative rate and minimise the false positive rate to prevent the algorithm from classifying possible clouds or sky brightness variations as a dust related image artefacts.
5. *Blob modelling.* We applied the optical model presented in Section 2.3 to estimate the size of the dust particles deposited on the ICC lens which produced each identified image artefact. For each validated blob, we retrieved the dust particle diameter, in units of length (μm), generating the model that best fit the segmented blob region of the ICC image using a non-linear least-squares minimisation method, implemented in the LMFIT library for Python (Newville et al., 2014). Only four parameters were required in the calculations: the focal length, $f$, the image or object distance, $s'$ or $s$, the diameter of the entrance pupil, $a$, and the distance between the lens and the first principal point, $w$ (Willson et al., 2005). For the ICC, the values of $f = 5.58$ mm and $a = 0.37$ mm are reported in Maki et al. (2018); for $s'$, we used the effective focal length of the pin-hole camera model of MER Hazcams, with $s' = 5.584$ mm (Smith et al., 2001; Willson et al., 2005); and for the distance to the lens window, $w$, we also assumed the MER Hazcams value of $w = 25$ mm reported in Willson et al. (2005).

The outputs of the retrieval include the number of valid dust blobs, their location, and the size of each blob (diameter) in pixels (FWHM) and in units of length (μm), resulting from the optical model best fitting retrieval.

## 3. Results

### 3.1. Number of dust image artefacts

The number of detected and validated image artefacts in the

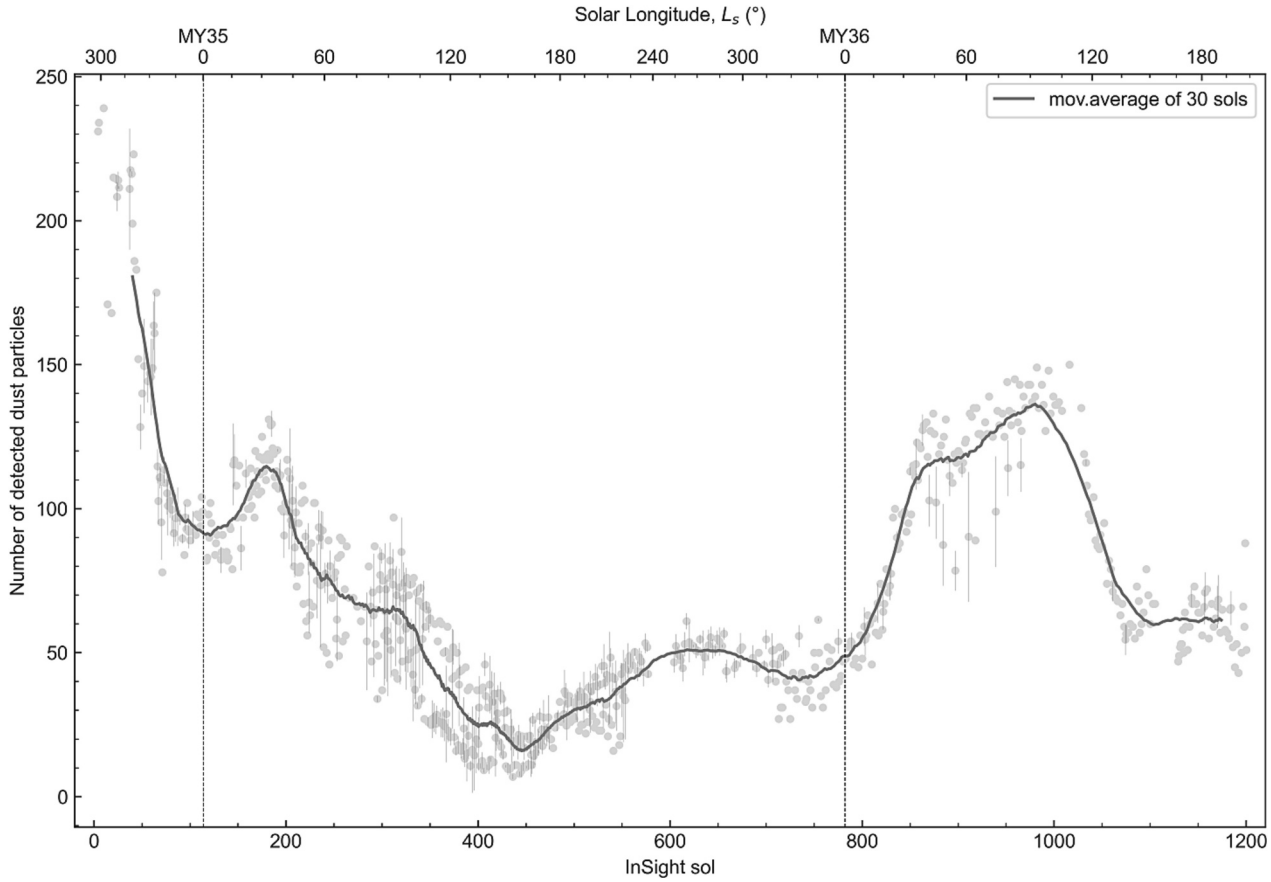


**Fig. 4.** Number of dust artefacts on ICC lens. Number of detected and validated image artefacts due to dust particles deposited on the ICC lens through the InSight mission. The first point of the graph corresponds to sol 4, LTST = 13:27:07, image file C000M0004_596888328EJP_F0000_0461M4, after the removal of the ICC lens protective cap. For those sols with multiple ICC observations available, the plotted data point corresponds to the mean of the detected dust blobs, while the error bar shows the standard deviation. The solid line corresponds to the moving average calculated for a 30-sol period.

evaluated sky region of ICC observation images due to dust particles deposited on the camera lens through the InSight mission is shown in Fig. 4.

The graph starts on sol 4 at LTST = 12:53:51 ($L_S$ = 298.1°), when then one-time deployable transparent cover for protecting the camera from dust and debris during the landing was removed (Maki et al., 2018). However, some of these dust particles deposited during landing onto the protective cap were transferred to the ICC lens after its deployment (Maki et al., 2019). In fact, while the number of dust artefacts detections at this time is around 250, results for the 4 previous observations with the cap on are around 475 (see full results in the supplementary material). The results show a period of high dust removal up to sol 65 to 70 ($L_S \sim$ 335.0°), when the number of counts reduces down to approximately 100, as it has been also reported in previous studies (Charalambous et al., 2021).

Except for the period with dust deposition and cleaning around sol ~160, the period starting from sol 70 shows a gradual removal of dust until sol ~450 ($L_S$ = 161.0°, MY35), when minima of around 10 detections are retrieved. This is followed by a gradual increase period when the number of detected particles varies up to about 50 around sol 800 ($L_S \sim$ 8.5°, MY36).

At sol ~800, the number of dust image artefacts on the ICC lens presents a remarkable increase, with particle counts varying from values of 50 counts up to 120 within a 50-sol period; which is then followed by a less prominent increase until sol ~975, when the maximum number of detected particles of ~150 counts is reached within the data series, excluding the initial accumulation due to landing.

Finally, after sol 1000 ($L_S$ = 101°) a moderate decay can be observed in the results until sol 1100 ($L_S$ = 150.2°), with a decay rate of 90 particles within a 100 sol-period. This decay reduced the average number of dust related image artefacts down to approximately 60, which remained more or less stable until the end of the evaluated data series at sol 1200 ($L_S$ = 207.7°).

### 3.2. Dust particle sizes

The result of the dust particle size estimations using the optics-based model proposed by Willson et al. (2005) presented in Section 2.3 is shown in Fig. 5.

A noticeable decay can be appreciated in dust particle diameters during the first 70 sols, following the same behaviour as the number of counts in Fig. 4. During the removal of dust particles deposited from landing, diameter values varied from an average of about 100 μm, with maximum of ~200 μm, retrieved for ICC's first observation on sol 0 (see full results in the supplementary material) down to mean values of around 80 μm on sol 4, after the removal of the camera lens protective transparent cap, which corresponds to the first data point of Fig. 5. At the end of this decay period around sol 70, the average diameters reduce down to approximately 50–55 μm.

The particle sizes remained roughly constant until sol ~325, when mean values drop from ~50 μm down to 40 μm, with minimum average values below 30 μm at some point around sol 450. It is worth mentioning that both the gradual decay in particle sizes within sols 325–450 and the period with minimum modelled particle sizes are in good agreement with the decrease in the number of blob counts detected and the following stable and clean period, respectively.

For the sol 800–1200 period, the results show an increase in the modelled particle size, with mean diameter values reaching approximately 55 μm, followed by a slight drop down to approximately 45 μm by sol ~1100 and finishing with fluctuations around this diameter size at sol 1200. Again, the estimated particle sizes within this period show a good agreement with the behaviour for the number of detected particles described in Fig. 4. Although in this case, a reduction of about 50% in the number of dust particle detections are paired with a variation of only 10 μm in particle sizes.

Regarding the size of the dust artefacts in the image-space, the resulting overall average particle diameter is of 18 ± 5 pixels. This result is in good agreement with findings reported for the optical model, where for dust particles smaller than the aperture area (0.37 mm for the ICC), the size of the image artefact is determined by the size of the lens aperture and not the size of the particle deposited on the lens; while the attenuation produced by the artefact is determined by the ratio of the particle and aperture areas (Willson et al., 2005).

### 3.3. Sensitivity analysis

A sensitivity analysis was performed in order to evaluate the influence of the model parameters and assumptions made on the resulting number of detected dust artefacts and estimated particle sizes.

In the potential dust blob detection and validation process, minimum and maximum blob radius values in the image space were set to $r_{min} = 3$ and $r_{max} = 15$ pixels, respectively. These parameters also influenced the width of the NCC template, defined as $2w = r_{min} + r_{max}$, while the other preset parameters in the template matching stage, $A_{min}$ = 1.0 DN and $\sigma_{NCC}$ = 0.8, had negligible impact on the number of detections. We performed additional retrievals for different pairs of ($r_{min}$, $r_{max}$) values of (3,20), (5, 15), and (5, 20). The comparison with the base retrieval showed in differences in the number of detected valid dust blobs of about −12%, −0.4% and − 16%, respectively, with resulting variations in the mean dust particle sizes of about +4.3%, +5.5%, and + 7.5%.

In the validation of the detected image artefacts as dust blob candidates, a minimum image brightness loss value of the resulting 2D-Gaussian fit of $A_{min}$ = 2 DN was derived empirically from the manual count analysis of the algorithm's performance for a subset of observations that covered different sols, periods, and under different illumination conditions. In order to evaluate the sensitivity of this parameter, further retrievals were performed for the same subset using minimum DN loss values of 1 and 3 DNs. The analysis of these retrievals showed a variation of the false negative rate of around −17% and + 23%, respectively, whereas the false positive rates varied respectively to +7% and − 9%. On the other hand, the estimated mean particle sizes showed overall variations of −4.2% and + 4.6%, respectively (for further details, see Section A2 of the supplementary material).

In the optics-based model presented in Section 2.3 and used for the estimation of the size of the dust particles deposited on the camera lens, an image space distance of $s'$ = 5.584 mm was selected based on the optical design report for the MER cameras (Smith et al., 2001) and following Willson et al. (2005), which after the relationship $1/s + 1/s' = 1/f$ resulted in an object space distance value of $s \sim$ 7.8 m. We performed further sensitivity analysis using the best focus value of $s$ = 0.5 m reported in Maki et al. (2018), which resulted in differences of about 7% in the retrieval of dust particle sizes. In addition, the distance between the camera lens and the entrance pupil for the ICC camera was assumed as $w$ = 25 mm, based on the value reported for the MER Hazcams (Willson et al., 2005). The sensitivity analysis of the particle size estimations for ±10% variations in this assumed distance value showed a negligible influence, with variations of <2.5%.

Following this, the maximum and minimum particle sizes that could be estimated using the optical model are estimated. Given the camera parameters, for dust particles smaller than the aperture area (0.37 mm for the ICC), the size of the blob is determined by the size of the lens aperture and not the size of the deposited dust particle, while the optical density of the blob is determined by the ratio of the particle and aperture areas (Willson et al., 2005). Since the output of the optical model is the optical density or amount of attenuation detected, the maximum detectable dust particle size is the one which causes a full attenuation, i.e. a pixel intensity of 0 DN, and corresponds to a diameter of ~369 μm. However, the minimum detectable deposited dust particle size depends on the background brightness (in DNs) of the 2$w$-sized blob evaluation kernel. A characteristic background brightness level was estimated by averaging the intensity of the central region of the image (rows 50 to 150 and columns 400 to 600) throughout all the ICC observations of the

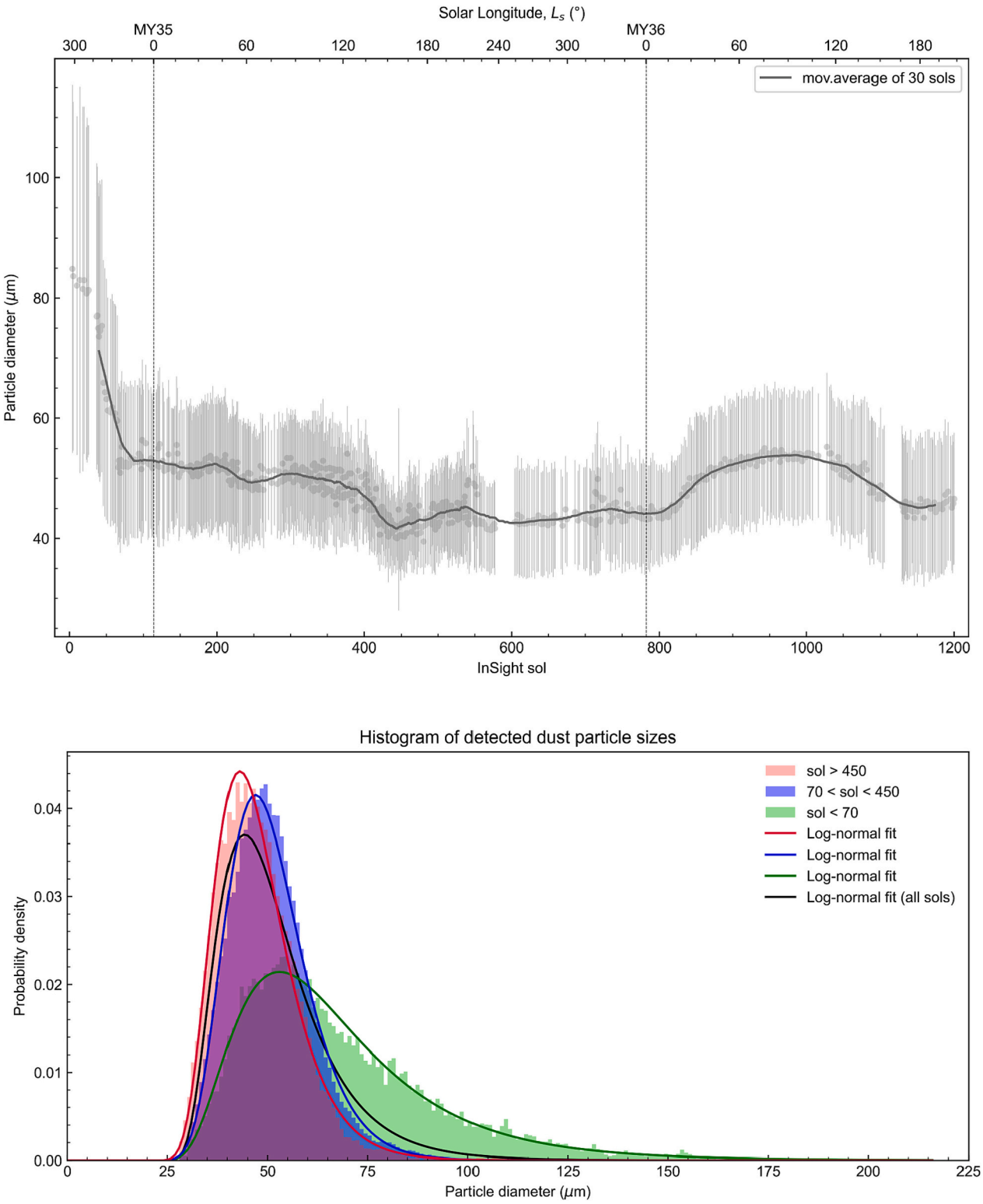


**Fig. 5.** Estimated dust particle sizes on ICC lens. Top panel: Mean of dust particle diameter estimated using the optics-based model for the detected image artefacts in ICC observations for each sol, with error-bars indicating the standard deviation, and the moving average calculated for a 30-sol period (solid line). The first data point of the plot corresponds to sol 4 (LTST = 13:27:07, image file C000M0004_596888328EJP_F0000_0461M4), the first observation retrieved after the removal of ICC's lens protective cap. Bottom panel: histogram of dust particle sizes of all retrievals and those retrieved during 3 different mission periods: sol 0 to 70, when dust particles deposited during the landing event were mostly removed, sol 70 to 450, minimum of detected dust particle counts, and post mission sol 450.

dataset, resulting in an overall average of 140 DN. Based on this, the minimum deposited dust particle size that would cause a decay of 1 DN from this level has an approximate diameter of 32 μm.

## 4. Discussion

While the full exploration of the aeolian processes and the various parameters influencing dust entrainment at InSight's landing site is beyond the scope of this work (see Newman et al., 2002; Baker et al., 2021; Charalambous et al., 2021; Lorenz et al., 2021a), a brief discussion is performed in this section to provide some context for the findings presented in this study regarding the observed periods of higher dust accumulation and removal activity and the mobilisation thresholds as a function of particle size.

### 4.1. Accumulation and removal

The overall gradual decay of the curve of detected number of dust particles deposited on the ICC lens shown in Fig. 4 is featured with two characteristic accumulation and removal periods: one starting around sol 160 and another during the sols 800–1100 period. Possible causes for the observed event around sol 160 may be related to the observed increase in the number of convective vortices reported at InSight from sol 160 until ~260, based on the detected dust devil tracks and surface darkening features, and the absence of activity thereafter (Charalambous et al., 2021),. In fact, the identified surface changes due to aeolian activity include 6 dust devil track detections between sols 164 and 203, with inferred peak wind speeds of 19 to 27 m/s (see Charalambous et al., 2021, Table 1). Further events were reported in the same study around sols 362 and 385, with measured wind speeds of ~31 m/s causing surface creeping, possible saltation and dust removal, based on the surface change analysis (Baker et al., 2021; Charalambous et al., 2021); however, no remarkable variations in the number of detections are observed on Fig. 4 within the vicinity of these sols. This is likely due to the low number of detections at that point in time, already close to the minimum, so these strong passing vortices would not have caused much cleaning on the ICC lens.

When comparing this decay between sols 250–425 with maximum daily wind speed records obtained by the TWINS meteorological suite instrument (Spiga et al., 2018, 2021; Baker et al., 2021), it can be appreciated a good correlation (anti-correlation). In fact, within this 175 sol period, a decrease in the number of detected particles of ~65 counts was retrieved while the measured maximum wind speeds showed an increase of up to 20 m/s. This could be a possible explanation for the sustained removal found during this period. Unfortunately, it was not possible to perform the same analysis for the dust accumulation and removal period between sols 800 and 1100, as TWINS pressure and wind measurements are not available or very limited after sol 760 (Spiga et al., 2021; InSight Seasonal Weather Report, 2022). If a seasonal behaviour of the previous events were assumed, with sols 160 and 362–385 corresponding respectively to $L_S \sim 23^\circ$ and 115–127° of MY35, extrapolating to the sols 800–1100 period ($L_S \sim$ 10–150°, MY36), as previously reported for InSight landing site (Charalambous et al., 2021) and observed on the MSL rover photodetectors (Vicente-Retortillo et al., 2018), dust devil activity occurring during the season might be a possible explanation to dust accumulation and removal within this period.

Regarding the interrelationship of dust accumulation and removal with atmospheric opacity, previous studies showed that for horizontal surfaces dust was observed to settle at rates proportional to the atmospheric optical depth, and to be removed in a number of discrete episodes (Kinch et al., 2007; Lorenz et al., 2021b). The atmospheric opacity retrievals at InSight's landing site (Spiga et al., 2018) show four main increases in the optical depth within the first 1000 sols period: a regional dust storm in with peak opacity values near $\tau = 2.0$ around sol 47 ($L_S = 324^\circ$) (Banfield et al., 2020; Lorenz et al., 2021a; Spiga et al., 2021), and three events with maximum opacity values of $\tau > 1.0$ and reaching 1.5, on sols 430, 580, and 710 (Lorenz et al., 2021a; InSight Seasonal Weather Report, 2022). The comparison of both the number of detections and variations in the detected particle sizes with atmospheric opacity values did not show any clear agreement with sol 47 (regional dust storm), 430, 580, and 710 events; although potential detections during the dust storm could be probably masked by the decay of dust particles deposited after landing. In fact, one of the largest cleaning events on the ICC lens as indicated by the differencing of sol 46–44 images (see Fig. 5b, c, of Charalambous et al., 2021) occurred during the early dust storm.

Previous results for vertically-oriented elements include the reported observations of dust cover on the MSL MAHLI calibration target (Yingst et al., 2020), where a mean dust coverage of 4.7% as a result of the balance of deposition and removal was found, with an estimated removal rate of 2–4% per sol. In addition, the evolution of dust coverage was not uniform with time, suggesting that the increase in the number of detected dust devils by the MSL rover during the second and third MY of the mission may have enhanced removal, but could also have been associated with higher deposition (Lorenz et al., 2021b). For the comparison of dust deposition on the vertically oriented ICC lens with the above-presented coverage results, we estimated the percentage of an ICC observation covered by dust particles as the ratio between the sum of the detected image artefact sizes, in pixels, and the number of non-masked pixels in the image. The ICC lens percentage cover values during the post-landing 10 sols are around 20–25%. These decreased down to ~15% in sol 100 once the deposited particles during landing were removed. An overall minimum value of 2% is estimated around sol 450, and during the sol 800–1100 accumulation and removal period, cover percentages increased from ~7% in sol 800 up to a maximum of 20% around sol 975, before decaying down to values of about 7% in sols 1100–1200. The overall mean dust coverage of ICC lens once the deposited particles during landing were removed is about 10 ± 4%.

### 4.2. Dust particle sizes

The particle size distribution of the detected dust particles deposited on the ICC lens is described in the histograms in Fig. 5 (bottom panel), together with their best fits to a log-normal distribution. The analysis of the estimated particle sizes of all the detected and validated image artefacts due to dust particles in the ICC observations database (around ~135,000 detections) returns an overall particle size distribution characterised by a mean diameter value of 52 ± 15 μm. If we break down this particle size distribution, in order to make some distinctions between the particles deposited during the landing event, the remaining particles after the prominent removal taking place within the first 70 sols, and further deposited dust after the minimum number of detections was reached around sol 450, we obtain three different particle size distribution histograms (Fig. 5, bottom panel) with average and standard deviation values of 65 ± 11 μm, 50 ± 4 μm, and 46 ± 4 μm, respectively. It can be appreciated from these results that large particles were mainly deposited during the landing event, while dust particles deposited later due to wind-driven processes are smaller in overall. The retrieved larger mean particle larger sizes for the first sols deposited by the effect of the retrorockets is consistent with grain size population estimations for InSight's landing site, with particles sizes of ~60 to 250 μm (classified as medium to very fine sand), as derived from pre-landing predictions based on remote sensing data from candidate landing sites and fragmentation theory (Golombek et al., 2017; Morgan et al., 2018; Charalambous, 2014), which were consistent with refined in-situ estimations based on radiometer data, imaging and fragmentation theory (Golombek et al., 2020a, 2021; Charalambous, 2014) and orbital-based thermal inertia measurements (Golombek et al., 2020c). On the other hand, the low levels of surface activity reported in Baker et al. (2021) and Charalambous et al. (2021) suggest that, rather than local saltators, the mean particle size for the later period could be more indicative of transported

particles.

Regarding the relationship between the estimated particle sizes and the number of detected particles, we have evaluated the possible effects of dust particle redistribution on the lens, i.e. coherence and disaggregation, which was previously seen on both the lander and surface (aggregation), as well as on the WTS shield after the passage of a convective vortex (disaggregation), as reported in Charalambous et al. (2021). The visual inspection of ICC images showed clear dust redistribution only during the 2–3 first ICC images, on the upper right-corner of the protective cap. The retrieval results showed a slight increase of the number of detected particles and the decrease of the mean value of particle sizes. However, no further clear signs of aggregation could be appreciated in the rest of the evaluated images (see supplementary material).

Lastly, a discussion is done in the next lines regarding the uncertainties associated to the assumption made of spherical discrete particles for representing the image artefacts due to deposited dust particles on the lens. The review of the contrast enhanced ICC observations, especially during the first 70 sols, showed that the majority of the particles deposited as discrete round-shaped grains, whereas irregularly large aggregates could be only detected in those observations when the ICC lens' protective cap was still on. Throughout the mission, the evaluated image artefacts corresponding to deposited small grains became fainter, and with no image artefacts migration (coherence or aggregation) evidences being detected.

### 4.3. Mobilisation thresholds

In order to evaluate possible sources of dust accumulation and removal on the ICC lens, the retrieved dust particle size range been evaluated with three different models of sediment mobilisation (e.g., Kahre et al., 2017; Kok et al., 2012): saltation (Shao and Lu, 2000), surface creeping/rolling (Merrison et al., 2007), and vortex-induced lifting (Greeley and Iversen, 1985). The modelled fluid thresholds obtained for saltation (Shao and Lu, 2000) and surface creeping (Merrison et al., 2007) have been extrapolated to wind speed $u$ at the height of $z \sim 1.2$ m of the wind sensor booms of the TWINS meteorological suite onboard the lander (Banfield et al., 2020; Golombek et al., 2020a, 2020b) by assuming that the near-surface wind follows a logarithmic profile with height in the form of (e.g. Prandtl, 1935; Bagnold, 1941; Greeley and Iversen, 1985; Sullivan et al., 2000):

$$u(z) = \frac{u^*}{k} \, ln\frac{z}{z_0} \tag{3}$$

where $k$ is the von Kármán constant ($k = 0.4$), and $z_0$ is the aerodynamic surface roughness, which controls the boundary layer of the wind profile. In situ estimations of this parameter for the InSight mission reported spatially highly heterogeneous values, varying from $z_0 \sim 0.01$ cm for the smooth east-southeast region to values of $z_0 \sim 0.1$ cm in the rougher terrain of the southwest to northwest, and up to $z_0 \sim 1$ cm in the instrument deployment area (see Charalambous et al., 2021).

In Fig. 6 we show the threshold curves for the three transport modes

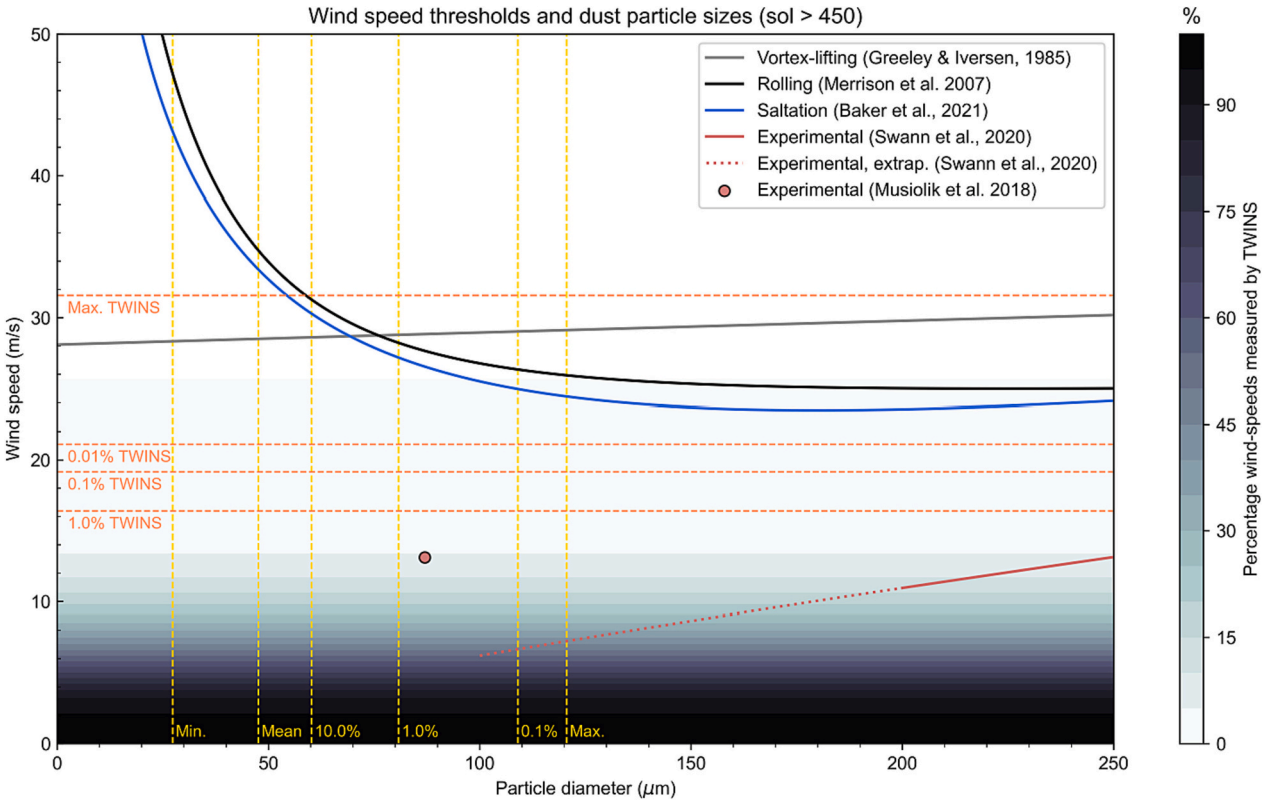


**Fig. 6.** *Minimum wind speed thresholds required to initiate motion.* Calculated theoretical fluid thresholds for vortex lifting (Greeley and Iversen, 1985), creeping (Merrison et al., 2007), and saltation (Baker et al., 2021), as a function dust particle size. Experimental fluid thresholds obtained for saltation under Mars gravity conditions by Musiolik et al. (2018) and the extrapolated sporadic motion thresholds derived from wind-tunnel measurements by Swann et al. (2020) are also included. The horizontal coloured region shows the percentile of wind-speeds measurement records by TWINS during daytime (LTST 06:00 to 18:00) since landing. The maximum wind observations retrieved by the Viking Lander 2 (VL2), Mars Science Laboratory (MSL) and InSight missions are also indicated, together with the mean wind speed during the regional dust storm in InSight sol 47 reported by Spiga et al. (2021). The vertical yellow lines represent different representative values of the dust particle size distribution retrieved from ICC observations for InSight mission sols >450. These representative values include: the minimum, mean and maximum particle sizes, as well as the particle sizes of the percentiles 90%, 99%, and 99.9%. (For interpretation of the references to colour in this figure legend, the reader is referred to the web version of this article.)

in the dust particle size range region estimated in this study. For this discussion, we have considered only those particles present in the ICC lens after sol 70, the moment when we assumed that all the larger dust particles (grains) deposited during the landing and post-landing have been effectively removed from the camera lens. It can be appreciated that both the daytime (LTST 6:00 to 18:00 h) wind-speeds collected by TWINS during the mission and the estimated particle sizes are below the theoretical models wind-speed thresholds, as previously reported by other authors (Sullivan et al., 2000; Perko et al., 2002; Swann et al., 2020), and in line with the low levels of surface activity observed at InSight (Baker et al., 2021; Charalambous et al., 2021).

It can be observed that, while the most easily mobilised particles are expected to be over the 100 μm diameter region, negligible signs of this (below 0.1%) are observed on the lens after sol 450, likely due to gravity effects or reduced saltation heights. This is in contrast with the post-landing period, when a large amount of particles with diameters above 75 μm and up to 200 μm were retrieved, which suggests that the deposition of such larger particles was due to the retrorockets' plume, rather than to wind-driven processes.

In Fig. 6, we have also considered the experimental measurements by Musiolik et al. (2018), which were retrieved under Martian gravity conditions during a parabolic flight, and wind-tunnel measurements by Swann et al. (2020). It can be appreciated that these experimental mobilisation thresholds are lower than those predicted by the theoretical models by a factor of 1.6 and up to 2.5 (Swann et al., 2020). By comparing with TWINS wind records and retrieved particle sizes, these models would suggest high surface change activity at InSight's landing site. However, while this might be valid on other sites of Mars with predominant strong unidirectional winds, such surface activity has not been observed at InSight, with rare and vortex-dependent aeolian changes (Baker et al., 2021; Charalambous et al., 2021) and lack of solar array panels cleaning events (Lorenz et al., 2020).

Regarding the small end of the particle size distribution, the particles deposited on the lens could be dust aggregates, which are more easily lifted and transported (e.g. Merrison et al., 2007), and subsequently adhere on the lens preferentially due to the force of the electrostatic charge (Perko et al., 2002; Edgett et al., 2015; Yingst et al., 2020). In this regard, dust particles that accumulate on the lens after sol 450 may have travelled long distances, but not global as these are not <10 μm airborne dust, in which case local wind speeds estimates at InSight may not be relevant for motion threshold comparisons.

## 5. Summary and conclusions

In this study we used images obtained by the ICC colour camera onboard the InSight lander to evaluate the accumulation and removal of dust on the camera lens and to estimate the size of the dust particles deposited on the lens window. The ICC is a 124° × 124° FOV fisheye lens camera mounted on the lander body underneath the top deck and pointing at the InSight mission instrument deployment area.

We evaluated ~2500 regularly-retrieved observations available in the PDS Imaging Node database, covering InSight mission sols 0 to 1200 (>1.5 Martian Years). For each observation, we have located and segmented the image artefacts due to dust particles using a template matching based blob detection method and evaluated the potential dust blobs with a 2-dimensional Gaussian loss model. The validated blobs were modelled using a first-order optical model in order to retrieve the dust particle size generating the best fitting model to the segmented image artefact area of the ICC image. A total number of about 135,000 image artefacts compatible with deposited dust on ICC lens were identified and validated for 743 different sols, obtaining an average modelled estimated diameter size of 52 ± 15 μm.

The analysis of the variation in the number of detected particles through the InSight mission show a deep removal period of dust particles deposited during the landing and post-landing until sol 70 ($L_S$ = 295–337°, MY34), followed by a moderate cleaning period until approximately sol 450 ($L_S$ = 160°, MY34), when the minimum number of detections were observed. The period between sols 450 and 800 ($L_S$ = 9°, MY36) shows a limited increase in the amount of accumulated dust, in contrast to the first quarter of MY36 (sols 800 to 950), with further steep increases and reaching values obtained during the initial period. The last observations of the evaluated dataset show a moderate to steep removal period between $L_S$ = 120–150°, MY36, followed by a stable period during the end of the evaluated series at sol 1200 ($L_S$ = 208°, MY36). The trend of the estimated dust particle sizes is similar to the number of detected particles, with larger particles, with diameters >100 μm and up to 200 μm, observed within the first 70 sols, deposited during the landing. Afterwards, particle sizes vary from average inferred values of 40 to 50 μm following the behaviour of the number of detected particles.

We identified two noticeable accumulation and removal periods around sol 160 and within the sol 800–1100 period, in addition to the removal stage of dust particle deposited during landing. The comparison with dust devil search campaigns reports suggest that the first event could be related to the passage of dust devils in the landing site vicinity. We evaluated InSight TWINS meteorological suite wind speed records and ICC estimated particle sizes with theoretical fluid thresholds models for sediment mobilisation under saltation, surface creeping and vortex-induced lifting. The comparison shows that both parameters are well below the theoretical model thresholds, although experimentally derived thresholds under Martian conditions with a unidirectional wind configuration have shown that these may be slower by a factor of up to 2.5. In such cases, the wind speeds and particles sizes may meet the requirements for an intermittent, sporadic motion. However, this contrast the paucity of surface activity at InSight, with rare and vortex-dependent aeolian activity, and lack of solar panel array cleaning events reported by previous studies.

The results of this study provide an additional source of observational data for evaluating aeolian dust processes in Mars, with quantitative results on dust accumulation and removal activity, and may contribute to a better tuning of dust entrainment threshold models by constraining susceptible dust particle sizes. In addition, the characterisation of dust particles deposited in the camera lens may contribute to the development of dust removal technologies and implementation of dust mitigation strategies, as a critical part of future Mars surface mission planning and operations.

Further research prospects derived from this study may include improvements in the detection and validation of image artefacts due to dust particles on the camera lens by means of convolutional neural networks and support vector machine (SVM) methods, as well as the implementation of algorithms for the removal of the image artefacts in order to mitigate the effects of the deposited dust on rover engineering cameras and affecting Mars surface mission activities.

## Declaration of Competing Interest

None.

## Data availability

Data will be made available on request.

## Acknowledgements

This work was supported by the Spanish project PID2019-109467GB-I00 (MINECO/FEDER, UE), Grupos Gobierno Vasco IT1742-22, and Diputación Foral de Bizkaia - Aula EspaZio Gela. J. Peralta thanks EMERGIA funding from Junta de Andalucía Spain (code: EMERGIA20_00414). The InSight Instrument Context Camera (ICC) observation files and labels used in this study are available at the InSight Cameras Online Data Bundle of NASA Planetary Data System (PDS) Imaging Node (https://pds-imaging.jpl.nasa.gov/data/nsyt/insight

_cameras/).

## Appendix A. Supplementary data

Supplementary data to this article can be found online at https://doi.org/10.1016/j.icarus.2022.115393.

## References


Arvidson, R.E., Guinness, E.A., Moore, H.J., Tillman, J., Wall, S.D., 1983. Three Mars years: Viking lander 1 imaging observations. Science 105 (17), 6222–6226. https://doi.org/10.1073/pnas.0800202105.

Arvidson, R.E., Gooding, J.L., Moore, H.J., 1989. The Martian surface as imaged, sampled, and analyzed by the Viking landers. Rev. Geophys. 27 (1), 39–60. https://doi.org/10.1029/RG027i001p00039.

Bagnold, R.A., 1941. The Physics of Blown Sand and Desert Dunes. Methuen, London, p. 265.

Baker, M., Newman, C., Charalambous, C., Golombek, M., Spiga, A., Banfield, D., Lemmon, M., Banks, M., Lorenz, R., Garvin, J., Grant, J., Lewis, K., Ansan, V., Warner, N., Weitz, C., Rodriguez, S., 2021. Vortex-dominated aeolian activity at InSight's landing site, part 2: local meteorology, transport dynamics, and model analysis. J. Geophys. Res. Planet 126. https://doi.org/10.1029/2020JE006514 e2020JE006514.

Banerdt, W.B., Smrekar, S.E., Banfield, D., Giardini, D., Golombek, M., Johnson, C.L., Lognonné, P., Spiga, A., Spohn, T., Perrin, C., Stähler, S.C., Antonangeli, D., Asmar, S., Beghein, C., Bowles, N., Bozdag, E., Chi, P., Christensen, U., Clinton, J., Collins, G.S., Daubar, I., Dehant, V., Drilleau, M., Fillingim, M., Folkner, W., Garcia, R.F., Garvin, J., Grant, J., Grott, M., Grygorczuk, J., Hudson, T., Irving, J.C. E., Kargl, G., Kawamura, T., Kedar, S., King, S., Knapmeyer-Endrun, B., Knapmeyer, M., Lemmon, M., Lorenz, R., Maki, J.N., Margerin, L., McLennan, S.M., Michaut, C., Mimoun, D., Mittelholz, A., Mocquet, A., Morgan, P., Mueller, N.T., Murdoch, 2020. Initial results from the InSight mission on Mars. In: Nagihara, S., Newman, C., Nimmo, F., Panning, M., Pike, W.T., Pleasa, A.-C., Rodriguez, S., Rodriguez-Manfredi, J.A., Russell, C.T., Schmerr, N., Siegler, M., Stanley, S., Stutzmann, E., Teanby, N., Tromp, J., van Driel, M., Warner, N., Weber, R., Wieczorek, M. (Eds.), Nature Geoscience 13, 183–189. https://doi.org/10.1038/s41561-020-0544-y.

Banfield, D., Spiga, A., Newman, C., Forget, F., Lemmon, M., Lorenz, R., Murdoch, N., Viudez-Moreiras, D., Pla-Garcia, J., Garcia, R.F., Lognonné, P., Karatekin, Ö., Perrin, C., Martire, L., Teanby, N., Van Hove, B., Maki, J.N., Kenda, B., Mueller, N.T., Rodriguez, S., Kawamura, T., McClean, J.B., Stott, A.E., Charalambous, C., Millour, E., Johnson, C.L., Mittelholz, A., Määttänen, A., Lewis, S.R., Clinton, J., Stähler, S.C., Ceylan, S., Giardini, D., Warren, T., Pike, W.T., Daubar, I., Golombek, M., Rolland, L., Widmer-Schnidrig, R., Mimoun, D., Beucier, É., Jacob, A., Lucas, A., Baker, M., Ansan, V., Hurst, K., Mora-Sotomayor, L., Navarro, S., Torres, J., Lepinette, A., Molina, A., Marin-Jimenez, M., Gomez-Elvira, J., Peinado, V., Rodrigues-Manfredi, J.-A., Carcich, B.T., Sackett, S., Russell, C.T., Spohn, T., Smrekar, S.E., Banerdt, W.B., 2020. The atmosphere of Mars as observed by InSight. Nat. Geosci. 13, 190–198. https://doi.org/10.1038/s41561-020-0534-0.

Bradski, G., 2000. The OpenCV Library. Dr Dobb's Journal of Software Tools.

Briechle, K., Hanebeck, U.D., 2001. Template matching using fast normalized cross correlation. In: Proceedings Volume 4387, Optical Pattern Recognition XII. https://doi.org/10.1117/12.421129.

Canny, J., 1986. A computational approach to edge detection. IEEE Trans. Pattern Anal. Mach. Intell. 8, 679–714. https://doi.org/10.1109/TPAMI.1986.4767851.

Charalambous, C., 2014. On the Evolution of Particle Fragmentation with Applications to Planetary Surfaces. https://doi.org/10.25560/32780.

Charalambous, C., McClean, J.B., Baker, M., Pike, W.T., Golombek, M., Lemmon, M., Ansan, V., Perrin, C., Spiga, A., Lorenz, R.D., Banks, M.E., Murdoch, M., Rodriguez, S., Weitz, C.M., Grant, J.A., Warner, N.H., Garvin, J., Daubar, I.J., Hauber, E., Stott, A.E., Johnson, C.L., Mittelholz, A., Warren, T., Navarro, S., Sotomayor, L.M., Maki, J., Lucas, A., Banfield, D., Newman, C., Viúdez-Moreiras, D., Pla-García, J., Lognonné, P., Banerdt, W.B., 2021. Vortex-dominated aeolian activity at InSight's landing site, part 1: multi-instrument observations, analysis, and implications. J. Geophys. Res. Planet 126. https://doi.org/10.1029/2020JE006757 e2020JE006757.

Deen, R., Zamani, P., Abarca, H., Maki, J., Hall, J.R., 2020. InSight (NSYT) Project Software Interfrace Specification: Camera Experiment Data Record (EDR) and Reduced Data Record (RDR) Data Products, Version 3.4, JPL D-56937. Release date: October 1, 2020. https://pds-imaging.jpl.nasa.gov/data/nsyt/insight_cameras/document/NSYT_Cam_SIS_3.4.pdf.

Dirik, A.E., Sencar, H.T., Memon, N., 2008. Digital single lens reflex camera identification from traces of sensor dust. IEEE Trans. Inform. Forens. Secur. 3 (3), 539–552. https://doi.org/10.1109/TIFS.2008.926987.

Drube, L., Leer, K., Goetz, W., Gunnlaugsson, H.P., Haspang, M.P., Lauritsen, N., Madsen, M.B., Sørensen, L.K.D., Ellehoj, M.D., Lemmon, M.T., Morris, R.V., Blaney, D., Reynolds, R.O., Smith, P.H., 2010. Magnetic and optical properties of airborne dust and settling rates of dust at the Phoenix landing site. J. Geophys. Res. 115 https://doi.org/10.1029/2009JE003419. E00E23.

Edgett, K.S., Caplinger, M.A., Maki, J.N., Ravine, M.A., Ghaemi, F.T., McNair, S., Herkenhoff, K.E., Duston, B.M., Wilson, R.G., Yingst, R.A., Kennedy, M.R., Minitti, M.E., Sengstacken, A.J., Supulver, K.D., Lipkaman, L.J., Krezoski, G.M., McBride, M.J., Jones, T.L., Nixon, B.E., Van Beek, J.K., Krysak, D.J., Kirk, R.L., 2015. Curiosity's robotic arm-mounted Mars Hand Lens Imager (MAHLI): Characterization and calibration status. 0001, Malin Space Science Systems.

Ehlmann, B.L., Edgett, K.S., Sutter, B., Achilles, C.N., Litvak, M.L., Lapotre, M.G.A., Sullivan, R., Fraeman, A.A., Arvidson, R.E., Blake, D.F., Bridges, N.T., Conrad, P.G., Cousin, A., Downs, R.T., Gabriel, T.S.J., Gellert, R., Hamilton, V.E., Hardgrove, C., Johnson, J.R., Kuhn, S., Mahaffy, P.R., Maurice, S., McHenrry, M., Meslin, P.-Y., Ming, D.W., Minitti, M.E., Morookian, J.M., Morris, R.V., O'Connell-Cooper, C.D., Pinet, P.C., Rowland, S.K., Schröder, S., Siebach, K.L., Stein, N.T., Thompson, L.M., Vaniman, D.T., Vasavada, A.R., Wellington, D.F., Wiens, R.C., Yen, A.S., 2017. Chemistry, mineralogy, and grain properties at Namib and High dunes, Bagnold dune field, Gale crater, Mars: a synthesis of curiosity rover observations. J. Geophys. Res. Planet 122, 2510–2543. https://doi.org/10.1002/2017JE005267.

Fergason, R.L., Christensen, P.R., Bell III, J.F., Golombek, M.P., Herkenhoff, K.E., Kieffer, H.H., 2006. Physical properties of the Mars exploration rover landing sites as inferred from Mini-TES-derived thermal inertia. J. Geophys. Res. Planet 111. https://doi.org/10.1029/2005JE002583. E02S21.

Ferguson, D.C., Kolecki, J.C., Siebert, M.W., Wilt, D.M., 1999. Evidence for Martian electrostatic charging and abrasive wheel wear from the wheel abrasion experiment on the pathfinder sojourner rover. J. Geophys. Res. 104 (E4), 8747–8789. https://doi.org/10.1029/98JE02249.

Geissler, P.E., Sullivan, R., Golombek, M., Johnson, J.R., Herkenhoff, K., Bridges, N., Vaughan, A., Maki, J., Parker, T., Bell, J., 2010. Gone with the wind: Eolian erasure of the Mars rover tracks. J. Geophys. Res. 115 https://doi.org/10.1029/2010JE003674. E00F11.

Gennery, D.B., 2006. Generalized camera calibration including fish-eye lenses. Int. J. Comput. Vis. 68 (3), 239–266. https://doi.org/10.1007/s11263-006-5168-1.

Goetz, W., Pike, W.T., Hviid, S.F., Madsen, M.B., Morris, R.V., Hecht, M.H., Staufer, U., Leer, K., Sykulska, H., Hemmig, E., Marshall, J., Morookian, J.M., Parrat, D., Vijendran, S., Bos, B.J., El Maarry, M.R., Keller, H.U., Kramm, R., Markiewicz, W.J., Drube, L., Blaney, D., Arvidson, R.E., Bell III, J.F., Reynolds, R., Smith, P.H., Woida, P., Woida, R., Tanner, R., 2010. Microscopy analysis of soils at the Phoenix landing site, Mars: classification of soil particles and description of their optical and magnetic properties. J. Geophys. Res. 115 https://doi.org/10.1029/2009JE003437. E00E22.

Golombek, M.P., Haldemann, A.F.C., Simpson, R.A., Fergason, R.L., Putzig, N.E., Arvidson, R.E., Bell III, J.F., Mellon, M.T., 2008. Martian surface properties from joint analysis of orbital, earth-based, and surface observations. In: Bell III, J.F. (Ed.), The Martian Surface: Composition, Mineralogy and Physical Properties (Cambridge Planetary Sience). Cambridge University Press, Cambridge, pp. 468–498. https://doi.org/10.1017/CBO9780511536076.022.

Golombek, M., Kipp, D., Warner, N., Daubar, I.J., Fergason, R., Kirk, R.L., Beyer, R., Huertas, A., Piqueux, S., Putzig, N.E., Campbell, B.A., Morgan, G.A., Charalambous, C., Pike, W.T., Gwinner, K., Calef, F., Kass, D., Mischna, M., Ashley, J., Bloom, C., Wigton, N., Hare, T., Schwartz, C., Gengl, H., Redmond, L., Trautman, M., Sweeney, J., Grima, C., Smith, I.B., Skyanskiy, E., Lisano, M., Benardini, J., Smrekar, S., Lognonné, P., Banerdt, W.B., 2017. Selection of the InSight landing site. Space Sci. Rev. 211, 5–95. https://doi.org/10.1007/s11214-016-0321-9.

Golombek, M., Warner, N.H., Grant, J.A., Hauber, E., Ansan, V., Weitz, C.M., Williams, N., Charalambous, C., Wilson, S.A., DeMott, A., Kopp, M., Lethcoe-Wilson, H., Berger, L., Hausmann, R., Marteau, E., Vrettos, C., Trussell, A., Folkner, W., Le Maistre, S., Mueller, N., Grott, M., Spohn, T., Piqueux, S., Millour, E., Forget, F., Daubar, I., Murdoch, N., Lognonné, P., Perrin, C., Rodriguez, S., Pike, W. T., Parker, T., Maki, J., Abarca, H., Deen, R., Hall, J., Andres, P., Ruoff, N., Calef, F., Smrekar, S., Baker, M.M., Banks, M., Spiga, A., Banfield, D., Garvin, J., Newman, C. E., Banerdt, W.B., 2020a. Geology of the InSight landing site on Mars. Nat. Commun. 11, 1014. https://doi.org/10.1038/s41467-020-14679-1.

Golombek, M., Williams, N., Warner, N.H., Parker, T., Williams, M.G., Daubar, I., Calef, F., Grant, J., Bailey, P., Abarca, H., Deen, R., Ruoff, N., Maki, J., McEwen, A., Baugh, N., Block, K., Tamppari, L., Call, J., Ladewig, J., Stoltz, A., Weems, W.A., Mora-Sotomayor, L., Torres, J., Johnson, M., Kennedy, T., Sklyanskiy, E., 2020b. Location and setting of the Mars InSight Lander, instruments, and landing site. Earth Space Sci. 7 https://doi.org/10.1029/2020EA001248 e2020EA001248.

Golombek, M., Kass, D., Williams, N., Warner, N., Daubar, I., Piqueux, S., Charalambous, C., Pike, W.T., 2020c. Assessment of InSight landing site predictions. J. Geophys. Res. Planet 125. https://doi.org/10.1029/2020JE006502 e2020JE006502.

Golombek, M.P., Trussell, A., Williams, N., Charalambous, C., Abarca, H., Warner, N.H., Deahn, M., Trautman, M., Crocco, R., Grant, J.A., Hauber, E., Deen, R., 2021. Rock size-frequency distributions at the InSight landing site, mars, earth and space. Science 8. https://doi.org/10.1029/2021EA001959 e2021EA001959.

Greeley, R., Iversen, J.D., 1985. Wind as a Geological Process on Earth, Mars, Venus and Titan, Cambridge Planetary Science Series, vol. 4. Cambridge University Press, Cambridge.

Greeley, R., Arvidson, R.E., Barlett, P.W., Blaney, D., Cabrol, N.A., Christensen, P.R., Fergason, R.L., Golombek, M.P., Landis, G.A., Lemmon, M.T., McLennan, S.M., Maki, J.N., Michaels, T., Moersch, J.E., Neakrase, L.D.V., Rafkin, S.C.R., Richter, L., Squyres, S.W., de Souza Jr., P.A., Sullivan, R.J., Thompson, S.D., Whelley, P.L., 2006. Gusev crater: wind-related features and processes observed by the Mars exploration rover spirit. J. Geophys. Res. Planet 111 (E2). https://doi.org/10.1029/2005JE002491.

Herkenhoff, K.E., Golombek, M.P., Guinness, E.A., Johnson, J.B., Kusack, A., Richter, L., Sullivan, R.J., Gorevan, S., 2008. In situ observations of the physical properties of the Martian surface. In: Bell III, J.F. (Ed.), The Martian Surface: Composition, Mineralogy, and Physical Properties (Cambridge Planetary Science). Cambridge

University Press, Cambridge, pp. 451–467. https://doi.org/10.1017/CBO9780511536076.021.
Herkenhoff, K.E., Squyres, S.W., Arvidson, R.E., Cole, S.B., Sullivan, R., Yingst, A., Cabrol, N., Lee, E.M., Richie, J., Sucharski, B., Bell III, J.F., Calef, F., Chapman, M., Edgar, L., Franklin, B., Geissler, P., Hurowitz, J., Jensen, E., Johnson, J.R., Kirk, R., Lanagan, P., Leff, C., Maki, J., Mullins, K., Redding, B., Rice, M., Sims, M., Soderblom, L., Spanovich, N., Springer, R., Sunda, A., Vaughan, A., 2019. Overview of Spirit microscopic imager results. J. Geophys. Res. Planet 124 (2), 528–584. https://doi.org/10.1029/2018JE005774.
InSight Seasonal Weather Report, 2022. Mars Weather and Climate from the InSight Mission, Image Credits: NASA/JPL-Caltech/Cornell/CAB. https://mars.nasa.gov/insight/weather/. Accessed on 30th March.
Johnson, J.R., Grundy, W.M., Lemmon, M.T., 2003. Dust deposition at the Mars pathfinder landing site: observations and modeling of visible/near-infrared spectra. Icarus 163, 330–346. https://doi.org/10.1016/S0019-1035(03)00084-8.
Kahre, M.A., Murphy, J.R., Newman, C.E., Wilson, R.J., Cantor, B.A., Lemmon, M.T., Wolff, M.J., 2017. The Mars dust cycle. In: Haberle, R., Clancy, R., Forget, F., Smith, M., Zurek, R. (Eds.), The Atmosphere and Climate of Mars. Cambridge Planetary Science, Cambridge University Press, pp. 295–337. https://doi.org/10.1017/9781139060172.010.
Kinch, K.M., Sohl-Dickstein, J., Bell III, J.F., Johnson, J.R., Goetz, W., Landis, G.A., 2007. Dust deposition on the Mars exploration rover panoramic camera (Pancam) calibration targets. J. Geophys. Res. 112 https://doi.org/10.1019/2006JE002807. E06S03.
Kinch, K.M., Bell III, J.F., Goetz, W., Johnson, J.R., Joseph, R., Madsen, M.B., Sohl-Dickstein, J., 2015. Dust deposition on the decks of the Mars exploration rovers: 10 years of dust dynamics on the panoramic camera calibration targets. Earth Space Sci. 2, 144–172. https://doi.org/10.1002/2014EA000073.
Kok, J.F., Parteli, E.J.R., Michaels, T.I., Karam, D.B., 2012. The physics of wind-blown sand and dust. Rep. Prog. Phys. 75 https://doi.org/10.1088/0034-4885/75/10/106901, 106901.
Kroon, D., 2009. Numerical Optimization of Kernel Based Image Derivatives. Short Paper University Twente.
Landis, G.A., Jenkins, P.P., 2000. Measurements of the settling rate of atmospheric dust on Mars by the MAE instrument on Mars pathfinder. J. Geophys. Res. 105, 1855–1857. https://doi.org/10.1029/1999JE001029.
Landis, G.A., Herkenhoff, K., Greeley, R., Thompson, S., Whelley, P., the MER Athena Science Team, 2006. Dust and sand deposition on the MER solar arrays as viewed by the Microscopic Imager. In: 37th Annual Lunar and Planetary Science Conference, Abstract No. 1932.
Lemmon, M.T., Wolff, M.J., Smith, M.D., Clancy, R.T., Banfield, D., Landis, G.A., Ghosh, A., Smith, P.H., Spanovich, N., Whitney, B., Whelley, P., Greeley, R., Thompson, S., Bell III, J.F., Squyres, S.W., 2004. Atmospheric imaging results from the Mars exploration rovers: Spirit and opportunity. Science 306, 1753–1756. https://doi.org/10.1126/science.1104474.
Lemmon, M.T., Guzewich, S.D., McConnochie, T., de Vicente-Retortillo, A., Martínez, G., Smith, M.D., Bell III, J.F., Wellington, Jacob, S., 2019. Large dust aerosol sizes seen during the 2018 Martian global dust event by the curiosity rover. Geophys. Res. Lett. 46 https://doi.org/10.1029/2019GL084407.
Levine, J.S., Winterhalter, D., Kerschmann, R.L., 2018. Dust in the Atmosphere of Mars and its Impact on Human Exploration. Cambridge Scholars Publishing.
Lewis, J.P., 1995. Fast Normalized Cross-Correlation, Industrial Light & Magic.
Lindeberg, T., 1993. Detection salient blob-like image structures and their scales with a scale-space primal sketch: a method for focus-of-attention. Int. J. Comput. Vis. 11 (3), 283–318. https://doi.org/10.1007/BF01469346.
Lorenz, R.D., Lemmon, M.T., Maki, J., Banfield, D., Spiga, A., Charalambous, C., Barrett, E., Herman, J.A., White, B.T., Pasco, S., Banerdt, W.B., 2020. Scientific observations with the InSight solar arrays: dust, clouds, and eclipses on Mars, earth and space. Science 7. https://doi.org/10.1029/2019EA000992 e2019EA000992.
Lorenz, R.D., Lemmon, M.T., Maki, J., 2021a. First Mars year of observations with the InSight solar arrays: winds, dust devil shadows, and dust accumulation. Icarus 364, 114468. https://doi.org/10.1016/j.icarus.2021.114468.
Lorenz, R.D., Martínez, G.M., Spiga, A., Vicente-Retortillo, A., Newman, C.E., Murdoch, N., Forget, F., Millour, E., Pierron, T., 2021b. Lander and rover histories of dust accumulation on and removal from solar arrays on Mars. Planet. Space Sci. 207, 105337 https://doi.org/10.1016/j.pss.2021.105337.
Maki, J.N., Bell III, J.F., Herkenhoff, K.E., Squyres, S.W., Kiely, A., Klimesh, M., Schwochert, M., Litwin, T., Willson, R., Johnson, A., Maimone, M., Baumgartner, E., Collins, A., Wadsworth, M., Elliot, S.T., Dingizian, A., Brown, D., Hagerott, E.C., Scherr, L., Deen, R., Alexander, D., Lorre, J., 2003. Mars exploration rover engineering cameras. J. Geophys. Res. 108 (E12), 8071. https://doi.org/10.1029/2003JE002077.
Maki, J., Thiessen, D., Pourangi, A., Kobzeff, P., Litwin, T., Scherr, L., Elliott, S., Dingizian, A., Maimone, M., 2012. The Mars science laboratory engineering cameras. Space Sci. Rev. 170, 77–93. https://doi.org/10.1007/s11214-012-9882-4.
Maki, J.N., Golombek, M., Deen, R., Abarca, H., Sorice, C., Goodsall, T., Schwochert, M., Lemmon, M., Trebi-Ollennu, A., Banerdt, W.B., 2018. The color cameras on the InSight Lander. Space Sci. Rev. 214, 105. https://doi.org/10.1007/s11214-018-0536-z.
Maki, J., Trebi-Ollennu, A., Banerdt, B., Sorice, C., Bailey, P., Khan, O., Kim, W., Ali, K., Lim, G., Deen, R., Abarca, H., Ruoff, N., Hollins, N., Andres, P., Hall, J., the InSight Operations Team, 2019. Imaging from the InSight Lander, abs. 50th Lunar and Planetary Science Conference 2019, LPI Contrib. No. 2132, id. 2176.
Markiewicz, W.J., Sablotny, R.M., Keller, H.U., Thomas, N., Titov, D., Smith, P.H., 1999. Optical properties of the Martian aerosols as derived from imager for Mars pathfinder midday sky brightness data. J. Geophys. Res. 104 (E4), 9009–9017. https://doi.org/10.1029/1998JE900033.
Merrison, J.P., Gunnlaugsson, H.P., Nørnberg, P., Jensen, A.E., Rasmussen, K.R., 2007. Determination of the wind induced detachment threshold for granular material on Mars using wind tunnel simulations. Icarus 191, 568–580. https://doi.org/10.1016/j.icarus.2007.04.035.
Mohr, D.P., Knapek, C.A., Huber, P., Zaehringer, E., 2019. Algorithms for particle detection in complex plasmas. J. Imaging 5, 30. https://doi.org/10.3390/jimaging5020030.
Moore, H.J., Hutton, R.E., Clow, G.D., Spitzer, C.R., 1987. Physical properties of the surface materials at the Viking landing sites on Mars. In: USGS Numbered Series Professional Paper 1389. https://doi.org/10.3133/pp1389.
Morgan, P., Grott, M., Knapmeyer-Endrun, B., Golombek, M., Delage, P., Lognonné, P., Piqueux, S., Daubar, I., Murdoch, N., Charalambous, C., Pike, W.T., Müller, N., Hagermann, A., Siegler, M., Lichtenheldt, R., Teanby, N., Kedar, S., 2018. A pre-landing assessment of regolith properties at the InSight landing site. Space Sci. Rev. 214, 104. https://doi.org/10.1007/s11214-018-0537-y.
Musiolik, G., Kruss, M., Demirci, T., Schrinski, B., Teiser, J., Daerden, F., Smith, M.D., Neary, L., Wurm, G., 2018. Saltation under Martian gravity and its influence on the global dust distribution. Icarus 306, 25–31. https://doi.org/10.1016/j.icarus.2018.01.007.
Neubeck, A., Van Gool, L., 2006. Efficient Non-Maximum Suppression, Presented at the 18th International Conference on Pattern Recognition, 2006, ICPR'06, 3, pp. 850–855. https://doi.org/10.1109/ICPR.2006.479.
Newman, C.E., Lewis, S.R., Read, P.L., Forget, F., 2002. Modeling the Martian dust cycle, 1. Representations of dust transport processes. J. Geophys. Res. 107 (E12), 5123 6–1. https://doi.org/10.1029/2002JE001910.
Newville, M., Stensitzki, T., Allen, D.B., Ingargiola, A., 2014. LMFIT: Non-linear Least-Square Minimization and Curve-Fitting for Python. Zenodo. https://doi.org/10.5281/zenodo.11813.
Perko, H.A., Nelson, J.D., Green, J.R., 2002. Review of Martian dust composition, transport, deposition, adhesion, and removal. In: Proc. of Engineering, Infrastructure, and Sciences in Space 2002. ASCE Press. https://doi.org/10.1061/40625(203)25.
Perrin, C., Rodriguez, S., Jacob, A., Lucas, A., Spiga, A., Murdoch, N., Lorenz, R., Daubar, I.J., Pan, L., Kawamura, T., Lognonné, P., Banfield, D., Banks, M.E., Garcia, R.F., Newman, C.E., Ohja, L., Widmer-Schnidrig, R., McEwen, A.S., Banerdt, W.B., 2020. Monitoring of dust devil tracks around the InSight landing site, Mars, and comparison with in situ atmospheric data. Geophys. Res. Lett. 47 (10) https://doi.org/10.1029/20202GL087234 e2020GL087234.
Pike, W.T., Staufer, U., Hecht, M.H., Goetz, W., Parrat, D., Sykulska-Lawrence, H., Vijendran, S., Madsen, M.B., 2011. Quantification of the dry history of the Martian soil inferred from in situ microscopy. Geophys. Res. Lett. 38 https://doi.org/10.1029/2011Gl049896. L24201.
Pollack, J.B., Ockert-Bell, M.E., Shepard, M.K., 1995. Viking lander image analysis of Martian atmospheric dust. J. Geophys. Res. 100 (E3), 5235–5250. https://doi.org/10.1029/94JE026-40.
Prandtl, L., 1935. The mechanics of viscous fluids. In: Durand, W.F. (Ed.), Aerodynamic Theory III. Springer, Berlin.
Shao, Y., Lu, H., 2000. A simple expression for wind erosion threshold friction velocity. J. Geophys. Res. 105 (D17), 22437–22443. https://doi.org/10.1029/2000JD900304.
Sierra, E., Marrugo, A.G., Millán, M.S., 2017. Dust particle artifact detection and removal in retinal images. Opt. Pura Apl. 50 (4), 379–387. https://doi.org/10.7149/OPA.50.4.49075.
Smith, M.D., 2008. Spacecraft observations of the Martian atmosphere. Annu. Rev. Earth Planet. Sci. 36, 191–219. https://doi.org/10.1146/annurev.earth.36.031207.124334.
Smith, G.H., Hagerott, E., Scherr, L.M., Herkenhoff, K.E., Bell III, J.F., 2001. Optical Designs for the Mars '03 Rover Cameras, Proc. SPIE 4441, Current Developments in Lens Design and Optical Engineering II. https://doi.org/10.1117/12.449558.
Spiga, A., Banfield, D., Teanby, N.A., Forget, F., Lucas, A., Kenda, B., Rodriguez Manfredi, J.A., Widmer-Schnidrig, R., Murdoch, N., Lemmon, M.T., Garcia, R.F., Martire, L., Karatekin, Ö., Le Maistre, S., Van Hove, B., Dephant, V., Lognonné, P., Mueller, N., Lorenz, R., Mimoun, D., Rodriguez, S., Beucler, É., Daubar, I., Golombek, M.P., Bertrand, T., Nishikawa, Y., Millour, E., Rolland, L., Brissaud, Q., Kawamura, T., Mocquet, A., Martin, R., Clinton, J., Stutzmann, É., Spohn, T., Smrekar, S., Banerdt, W.B., 2018. Atmospheric science with InSight. Space Sci. Rev. 214, 109. https://doi.org/10.1007/s11214-018-0543-0.
Spiga, A., Murdoch, N., Lorenz, R., Forget, F., Newman, C., Rodriguez, S., Pla-Garcia, J., Viúdez-Moreiras, D., Banfield, D., Perrin, C., Mueller, N.T., Lemmon, M., Millour, E., Banerdt, W.B., 2021. A study of daytime convective vortices and turbulence in the Martian planetary boundary layer based on half-a-year of InSight atmospheric measurements and large-eddy simulations. J. Geophys. Res. Planet 126. https://doi.org/10.1029/2020JE006511 e2020JE006511.
Stella, P.M., Herman, J.A., 2010. The Mars surface environment and solar array performance. In: 2010 35th IEEE Photovoltaic Specialists Conference, 2010, 002631–002635. https://doi.org/10.1109/PVSC.2010.5617185.
Sullivan, R., Greeley, R., Kraft, M., Wilson, G., Golombek, M., Herkenhoff, K., Murphy, J., Smith, P., 2000. Results for the imager for Mars pathfinder windsock experiment. J. Geophys. Res. 105 (E10), 24547–24562. https://doi.org/10.1029/1999JE001234.
Swann, C., Sherman, D.J., Ewing, R.C., 2020. Experimentally derived thresholds for windblown sand on Mars. Geophys. Res. Lett. 47 https://doi.org/10.1029/2019GL084484 e2019GL084484.

The Rover Team, 1997. Characterization of the Martian surface deposits by the Mars pathfinder rover, sojourner. Science 278 (5344), 1765–1768. https://doi.org/10.1126/science.278.5344.1765.

Tomasko, M.G., Doose, L.R., Lemmon, M., Smith, P.H., Wegryn, E., 1999. Properties of dust in the Martian atmosphere from the imager on Mars pathfinder. J. Geophys. Res. 104, 8987–9007. https://doi.org/10.1029/1998JE900016.

Tsai, D.-M., Lin, C.-T., 2003. Fast normalized cross correlation for defect detection. Pattern Recogn. Lett. 24 (15), 2625–2631. https://doi.org/10.1016/S0167-8655(03)00106-5.

Van der Walt, S., Schönberger, J.L., Nunez-Iglesias, J., Boulogne, F., Warner, J.D., Yager, N., Gouillart, E., Yu, T., the scikit-image contributors, 2014. scikit-image: image processing in Python. PeerJ 2. https://doi.org/10.7717/peerj.453 e453.

Vaughan, A.F., Johnson, J.R., Herkenhoff, K.E., Sullivan, R., Landis, G.A., Goetz, W., Madsen, M.B., 2010. Pancam and microscopic imager observations of dust on the Spirit rover: cleaning events, spectral properties, and aggregates. Mars 5, 129–145. https://doi.org/10.1555/mars.2010.0005.

Vicente-Retortillo, A., Martínez, G.M., Renno, N., Newman, C.E., Ordonez-Etxberria, I., Lemmon, M.T., Richardson, M.I., Hueso, R., Sánchez-Lavega, A., 2018. Seasonal deposition and lifting of dust on Mars as observed by the curiosity rover. Sci. Rep. 8, 17576. https://doi.org/10.1038/s41598-018-35946-8.

Virtanen, P., Gommers, R., Oliphant, T.E., Haberland, M., Reddy, T., Cournapeau, D., Burovski, E., Peterson, P., Weckesser, W., Bright, J., van der Walt, S.J., Brett, M., Wilson, J., Millman, K.J., Mayorov, N., Nelson, A.R.J., Jones, E., Kern, R., Larson, E., Carey, C.J., Polat, İ., Feng, Y., Moore, E.W., VanderPlas, J., Laxalde, D., Perktold, J., Cimrman, R., Henriksen, I., Quintero, E.A., Harris, C.R., Archibald, A.M., Ribeiro, A.H., Pedregosa, F., van Mulbregt, P., SciPy 1.0 Contributors, 2020. SciPy 1.0: fundamental algorithms for scientific computing in Python. Nat. Methods 17 (3), 261–272. https://doi.org/10.1083/s41592-019-0686-2.

Willson, R.G., Maimone, M.W., Johnson, A.E., Scherr, L.M., 2005. An optical model for image artifacts produced by dust particles on lenses. In: Proc. of 'The 8th International Symposium on Artificial Intelligence, Robotics and Automation in Space - iSAIRAS' Conference, 5–8 September 2005, ESA SP-603.

Yakimovsky, Y., Cunningham, R., 1978. A system for extracting three-dimensional measurements from a stereo pair of TV cameras. Comput. Graph. Image Process. 7 (2), 195–210. https://doi.org/10.1016/0146-664X(78)90112-0.

Yen, A.S., Gellert, R., Schröder, C., Morris, R.V., Bell III, J.F., Knudson, A.T., Clarck, B.C., Ming, D.W., Crisp, J.A., Arvidson, R.E., Blaney, D., Brückner, J., Christensen, P.R., DesMarais, D.J., de Souza Jr., P.A., Economou, T.E., Ghosh, A., Hahn, B.C., Herkenhoff, K.E., Haskin, L.A., Hurowitz, J.A., Joliff, L., Johnson, J.R., Klingelhöfer, G., Madsen, M.M., McLennan, S.M., McSween, H.Y., Richter, L., Rieder, R., Rodionov, D., Soderblom, L., Squyres, S.W., Tosca, N.J., Wang, A., Wyatt, M., Zipfel, J., 2005. An integrated view of the chemistry and mineralogy of martian soils. Nature 436, 49–54. https://doi.org/10.1038/nature03637.

Yingst, R.A., Bray, S., Herkenhoff, K., Lemmon, M., Minitti, M.E., Schmidt, M.E., Edgett, K.S., Fey, D.M., Kah, L.C., 2020. Dust cover on Curiosity's Mars hand Lens Imager (MAHLI) calibration target: implications for deposition and removal mechanisms. Icarus 351, 113872. https://doi.org/10.1016/j.icarus.2020.113872.